227-90.RPT

HEATING OF A LIQUID/VAPOR MIXTURE BY A PULSED ELECTRIC DISCHARGE

GTD 90-7

Final Technical Report

August 31, 1990.

by

R.L. Burton
B.K. Hilko
F.D. Witherspoon

Prepared for:

Air Force Office of Scientific Research

Contract No. F49620-87-C-0061

Mitat A. Birkan, Program Manager

Period of Performance:

July 1, 1987 to June 30, 1990.

GT-Devices, Inc.,
5705A General Washington Dr.,
Alexandria, VA - 22312.

UNCLASSIFIED
SECURITY CLASSIFICATION OF THIS PAGE

REPORT DOCUMENTATION PAGE

Form Approved
OMB No. 0704-0188

1a. REPORT SECURITY CLASSIFICATION UNCLASSIFIED	1b. RESTRICTIVE MARKINGS
2a. SECURITY CLASSIFICATION AUTHORITY	3. DISTRIBUTION/AVAILABILITY OF REPORT Approved for public release; distribution unlimited.
2b. DECLASSIFICATION/DOWNGRADING SCHEDULE	
4. PERFORMING ORGANIZATION REPORT NUMBER(S) GTD 90-7	5. MONITORING ORGANIZATION REPORT NUMBER(S)
6a. NAME OF PERFORMING ORGANIZATION GT-Devices, Inc. — 6b. OFFICE SYMBOL (If applicable)	7a. NAME OF MONITORING ORGANIZATION Air Force Office of Scientific Research
6c. ADDRESS (City, State, and ZIP Code) 5705a General Washington Dr. Alexandria, VA - 22312	7b. ADDRESS (City, State, and ZIP Code) Bolling AFB Washington, DC - 20332-6448
8a. NAME OF FUNDING/SPONSORING ORGANIZATION AFOSR — 8b. OFFICE SYMBOL (If applicable) NA	9. PROCUREMENT INSTRUMENT IDENTIFICATION NUMBER Contract No. F49620-87-C-0061
8c. ADDRESS (City, State, and ZIP Code) AFOSR/NA Bolling AFB DC 20332-6448	10. SOURCE OF FUNDING NUMBERS PROGRAM ELEMENT NO. 61102F — PROJECT NO. 2308 — TASK NO. A1 — WORK UNIT ACCESSION NO.
11. TITLE (Include Security Classification) Heating of a Liquid/Vapor Mixture by a Pulsed Electric Discharge (U)	
12. PERSONAL AUTHOR(S) Rodney L. Burton, Brian K. Hilko, and F. Doug Witherspoon	
13a. TYPE OF REPORT Final Technical — 13b. TIME COVERED FROM 7/1/87 TO 6/30/90	14. DATE OF REPORT (Year, Month, Day) August 31, 1990. — 15. PAGE COUNT 72
16. SUPPLEMENTARY NOTATION	

17. COSATI CODES		
FIELD	GROUP	SUB-GROUP

18. SUBJECT TERMS (Continue on reverse if necessary and identify by block number)
Plasma discharge, Liquid vaporization, Spectroscopy, Numerical modeling

19. ABSTRACT (Continue on reverse if necessary and identify by block number)

A liquid fueled, pulsed electric discharge was studied to identify the energy exchange and mixing processes ocurring between the liquid, vapor, and plasma components. Liquid water, injected into a small bore (3.5-5.0 mm diameter) capillary tube, was subjected to power pulses of up to 5 MW for 15-60 μs duration. Experiments were performed with a variety of discharge and liquid injection conditions. A complex, highly transient sequence of heating and vaporization events occurs as revealed in detailed studies of the plasma optical emissions and resistivity. A 1-D, one fluid model was developed and numerical simulations were performed to help isolate the basic physical processes dominating the discharge dynamics.

20. DISTRIBUTION/AVAILABILITY OF ABSTRACT ☐ UNCLASSIFIED/UNLIMITED ☒ SAME AS RPT. ☐ DTIC USERS	21. ABSTRACT SECURITY CLASSIFICATION UNCLASSIFIED
22a. NAME OF RESPONSIBLE INDIVIDUAL Mitat A. Birkan	22b. TELEPHONE (Include Area Code) (202) 767-4938 — 22c. OFFICE SYMBOL NA

DD Form 1473, JUN 86 — Previous editions are obsolete. — SECURITY CLASSIFICATION OF THIS PAGE

(4)

TABLE OF CONTENTS

1.0 INTRODUCTION

Liquid-plasma discharges are of growing interest for the generation of high density, high enthalpy flows for rocket propulsion and wind tunnel test facilities. An electric propulsion system with an I_{sp} of 1000-3000 seconds is the pulsed electrothermal thruster (PET) being developed in our laboratory.[1] This device uses a high pressure (10^2 atm), modest temperature (1-1.5 eV) plasma generated in a capillary confined electric discharge (Fig. 1.1). In the PET scheme, liquid propellant (water) is injected into the capillary chamber through a small orifice at the cathode. A second device, currently in the prototype stage, is being designed to generate mach 10-20 air flows at 2-7 km/s for testing scramjet engines used on hypersonic aircraft.[2,3] The high enthalpy flow in this device will be created by injecting liquid air into the capillary and heating it with a 100 MW level discharge.

Arc discharge heaters in the 5-1000 MW class, used for pulsed electrothermal propulsion or hypersonic combustion research, are required to ingest their working fluid in solid or liquid form in order to keep working temperatures within the desired 6000-20,000 °K range. Plasma generation proceeds with the application of a high current (3-50 kA) heating pulse from a capacitive PFN or similar source. Critical to the understanding of these discharges is an experimental and theoretical investigation into the interaction of a cold liquid/vapor mixture and hot plasma present in the high power capillary environment.

A variety of complex, interdependent phenomena can participate in the energy transfer and mixing processes (Fig. 1.2). Plasma radiation, thermal conduction and convection all contribute to the heat flux for evaporation of the liquid. Vapor-plasma mixing can occur in the fast flow field as a steady surface erosion or via instabilities leading to a more-or-less explosive breakup of the injected liquid. This research effort seeks some understanding of these processes using liquid water injected into a 5 MW, 100 atm, capillary confined pulsed arc for which the arc heating is roughly constant in time. The goal is to identify in detail the dominant energy exchange and mixing processes occurring between the liquid, vapor and plasma components of the discharge.

Over the first year of this program we examined the behavior of these discharges by the application of spectroscopic and electrical diagnostics and obtained measurements of the time dependence of various plasma conditions such as density, temperature, pressure, and resistance.[4] During year two, the diagnostics were refined and extended to give a more detailed picture of the discharge dynamics.[5] Additionally, attention was shifted towards theoretical modeling and numerical simulation of the discharge.

This report outlines these earlier studies and incorporates the work performed during the final (third) year of the program. The model has been extended to include an empirical description of the plasma radiation environment along with detailed calculations of the plasma equilibrium composition, thermodynamic functions, and resistivity. Numerical simulations of several discharge configurations have been performed and the results are in excellent agreement with the experimental data.

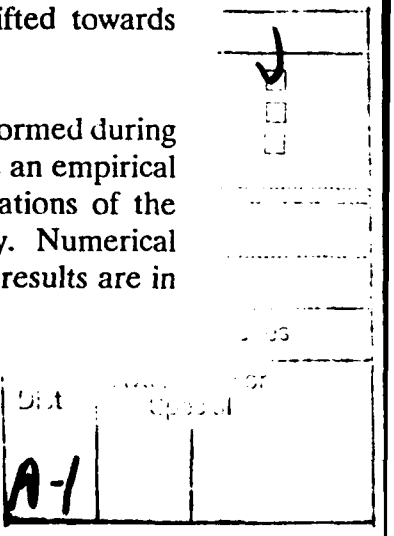

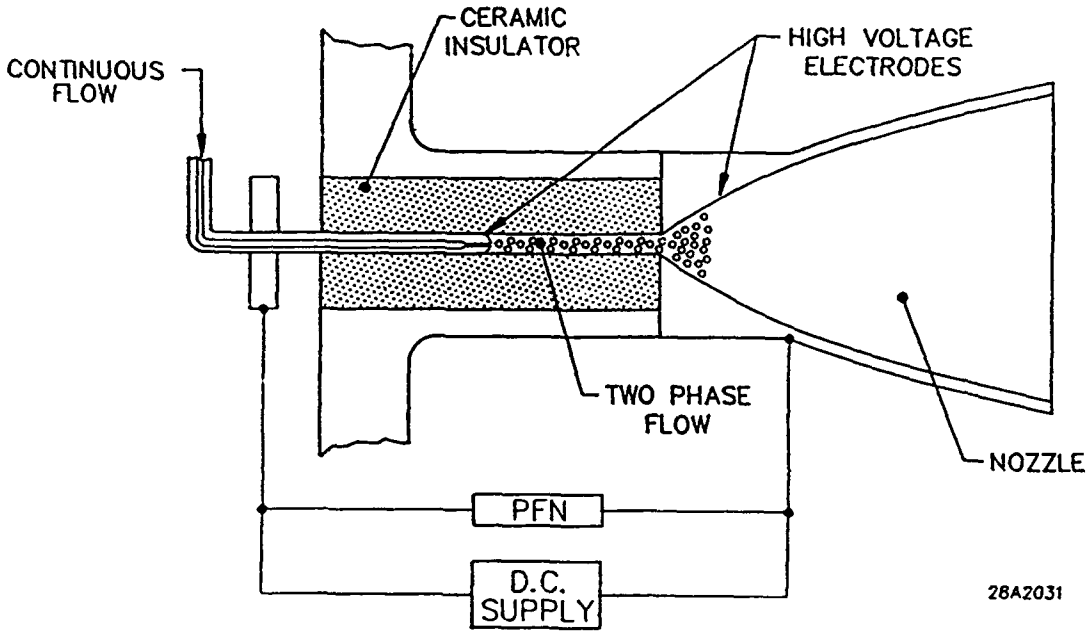

Figure 1.1 - Schematic of the repetitive pulsed electrothermal thruster (PET).

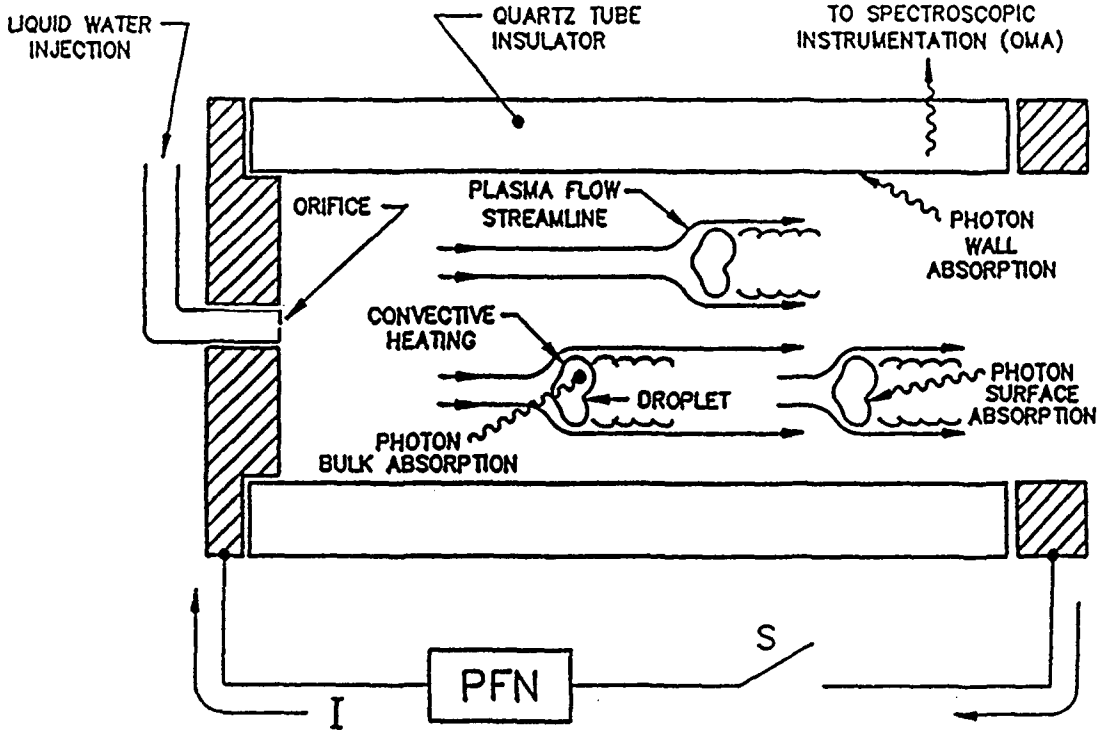

Figure 1.2 - Schematic of the liquid-vapor heating in a pulsed electric discharge.

2.0 SUMMARY

The experimental arrangement including PFN, capillary, and optical diagnostics are reviewed in Sec. 3. The parameter domains studied include i) driving pulse durations of 15-60 μs, ii) a survey of power loading effects using discharge currents of 3-6 kA, iii) a 25:1 difference in the liquid surface area using straight jet vs water wall injection schemes, and iv) the use of other capillary materials, e.g. polyethylene, without water injection, to examine other "fuels".

Detailed data for the resistance-time behavior are presented in Sec. 4. This data reveals a complex sequence of events. An early time high temperature, low resistance phase is followed by vaporization of the liquid surface and increased resistance as the plasma cools. Due to the density dependence of resistivity, a subsequent decrease in resistance is observed as the plasma density builds up inside the capillary. The resistance modulations are seen to be general characteristics of these wall confined discharges. Details of the transients do depend strongly on such things as power loading, fuel material, etc. Experiments with 60 μs pulse durations indicate that quasi-steady state conditions are reached in times $t \leq 30$ μs.

Several optical methods were employed to study the discharge (Secs. 5 and 6). Broadband photodiode observations and low resolution spectroscopy demonstrate that wall ablation and a transition to optically thick plasma conditions occurs within 5-15 μs. In low power density discharges it was possible to determine the plasma temperature from high resolution measurements of OII and OIII emission lines. The method assumes an LTE plasma where the line intensities are proportional to the upper level populations which follow a Boltzmann distribution, i.e. $I \propto \exp(-E_u/kT)$. The intensity ratio of lines from successive ionization stages gives a sensitive measure of temperature, though the electron density must be independently established. A relatively hot plasma of temperature T ~ 3-4 eV is seen at early times ($t < 10$ μs) with subsequent cooling to $T < 2$ eV.

In Sec. 6 we present nitrogen laser shadography experiments that show the liquid water droplets shattering in the fast axial flow of the exhaust plasma. The significance here is that the capillary model uses a 1-D, one fluid (plasma) description of the discharge where the liquid and vapor are not explicitly treated as seperate components of the flow. Processes such as droplet shattering, leading to radial dispersion and/or surface area enhancements,were assumed not to play an important role in determining the discharge dynamics. This assumption appears quite reasonable within the domain of the present experiments though the importance of droplet breakup, especially in higher power, longer duration discharges, has not been thoroughly investigated.

Third year efforts focussed on improving the physics model and performing numerical simulations of the discharge (Sec. 7). The fluid equations are solved for a one dimensional discharge chamber and drift tube section using a flux corrected transport (FCT) algorithm. Preliminary simulations used a very simple description of the discharge to examine the time scales over which various fluid parameters approach steady state conditions. Under constant

current, constant resistance conditions, the plasma temperature responds quickly (~5 μs) while pressure or density require ~40 μs to stabilize. The simple model did not adequately describe the measured resistance variations and several refinements were studied. At present the model incorporates the following basic features.

1) The current pulses input to the code were taken directly from the experimental data.
2) In order to cover a broad range of temperatures, the plasma resistivity was calculated from a modified Spitzer formula where both electron-ion and electron-neutral collisions are taken into account. The time variation of $Z\ln\Lambda$ is also important during build-up of the density.
3) Vaporization occurs at the liquid surface as a steady surface erosion with a rate determined by the local heat flux q.
4) Plasma radiation was assumed to dominate the heat flux while that due to thermal conduction or turbulent transport was assumed negligible. Using $q = \sigma T^4$ presumes the plasma to radiate as a pure blackbody though it was necessary to incorporate the fact that the plasma transitions from optically thin to thick during the power pulse.
5) The composition and thermodynamic properties of a water plasma were calculated in detail from the system of Saha equations (Appendix). Molecular species were not accounted for at low temperatures while, at high temperatures, up to triply ionized oxygen species were considered.

The model was evaluated primarily by comparing the resistance data obtained experimentally with the simulation results. An excellent match is obtained for both the magnitude and dynamic behavior of the resistance of all water discharges studied. Other measured parameters such a temperature, pressure, and axial variation in resistance show good agreement with the simulations. Section 7 includes the simulation results and detailed comparisons with the available experimental data.

Conclusions of the present study are presented in Sec. 8 where it is noted that the present model is sufficiently well developed to give confidence in our design and predictive capabilities for these capillary discharges.

3.0 EXPERIMENTAL ARRANGEMENT

This section provides basic documention relating to the subsystem components of the experiment. The general characteristics, nominal operating parameters and system layout are summarized below. Additional details are given in previous interim reports.[4,5]

3.1 Capillary Structure

The capillary assembly and individual components are shown in Figs. 3.1 and 3.2. A vacuum feedthrough shaft, 3/4" outside diameter, was constructed as a coaxial conductor. The center conductor was drilled through to form part of the water injection line. The discharge chamber itself was fused quartz tubing (GE type 214) measuring 10 mm OD x 40 mm long with an inner diameter of either 5.0 mm or 3.5 mm. Slots were made in the outer return conductor to give direct visual access to the discharge plasma. Water was injected from the cathode end through a 200 μm diameter pinhole. At the exhaust end a screw-on cap clamped the components together and also serves as the discharge anode. A transitioning or nozzle profile was not incorporated in the end cap so that the plasma undergoes a free expansion into the vacuum chamber.

In recent studies, the above capillary structure was modified to enable resistance measurements to be made with resolution in the axial direction. The Maycor structure of Fig. 3.3 has steel pins of 1/16" diameter inserted radially at 3/8" intervals along the capillary length. At the OD of the Maycor, the pins are held in place with epoxy while the interior ends are flush with the bore and make electrical contact with the plasma. The anode, capillary, and feedthrough shaft are clamped together with threaded rods which also serve to form an approximately coaxial current return path.

3.2 Water Injection

Various jet and spray injection conditions were avaliable. The experiments described in this report were performed using either the straight jet, or so-called water wall injection schemes. The straight jet is essentially a continuous cylinder of water injected along the axis of the discharge chamber and having a diameter equal to that of the pinhole. The water wall configuration was obtained by injecting a highly divergent spray of water droplets. The spray impinges on the capillary wall within a few millimeters of the cathode and subsequently forms a uniform, thin film of water flowing along the wall.

A continuous flow of water was maintained in the capillary using a simple blowdown arrangement. Excess water was pumped from the vacuum chamber. Under normal operating conditions an ambient pressure of 4.5-5.0 torr water vapor is maintained. The mass of water resident in the capillary on each shot is well defined and determined only by the pinhole size. A 200 μm diameter pinhole injects 0.31 mg/cm of capillary or 1.4 mg total in the discharge chamber. Typical jet velocities are only a few meters per second so that on the discharge time scales the water is essentially a stationary mass fill. It is worth pointing out

REVISIONS			
REV.	DESCRIPTION	DATE	APPROVED

NOTES:

1. REFERENCE DWG 13S-2-003

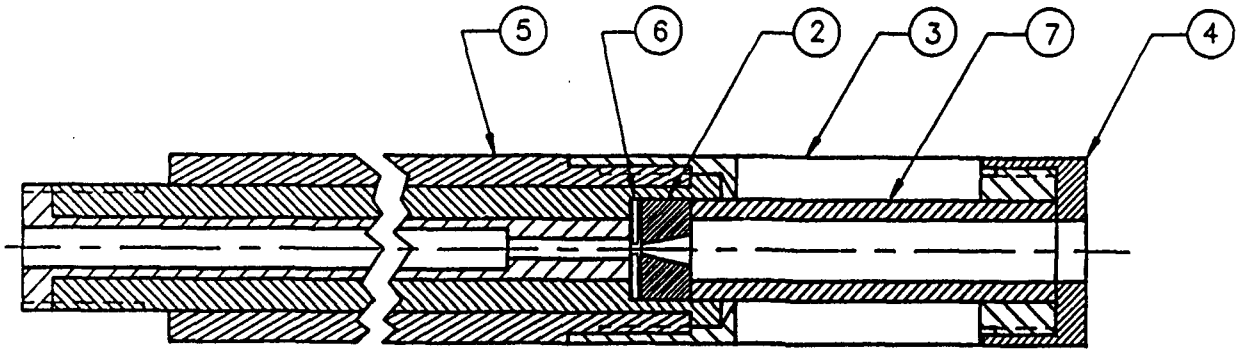

7	1			CAPILLARY	QUARTZ
6	1			PINHOLE ORIFICE	SST
5	1		28B-1-012	FEEDTHROUGH	SEE NOTE 1
4	1		28B-1-011	END CAP	SST
3	1		28B-1-010	CAPILLARY CONTAINMENT	SST
2	1		28B-1-009	CATHODE	CMW 1000
1	1		28B-1-008	ASSEMBLY	
	QTY REQD	CODE IDENT	PART OR IDENTIFYING NO.	NOMENCLATURE OR DESCRIPTION	MATERIAL SPECIFICATION

PARTS LIST

	PET-P
NEXT ASSY	USED ON
APPLICATION	

UNLESS OTHERWISE SPECIFIED DIMENSIONS ARE IN INCHES
TOLERANCES ARE:
FRACTIONS ± DECIMALS .XX ± .01 .XXX ± .005 ANGLES ± °

MATERIAL SEE PL

FINISH

DO NOT SCALE DRAWING

CONTRACT NO.

APPROVALS	DATE
DRAWN AG	10/12/87
CHECKED	
ISSUED	

GT-DEVICES

ASSY, CAPILLARY

SIZE B | FSCM NO. | DWG. NO. 28B-1-008 | REV.

SCALE 1/1 | SHEET

Figure 3.1 - Sectional view of the feedthrough and capillary assembly.

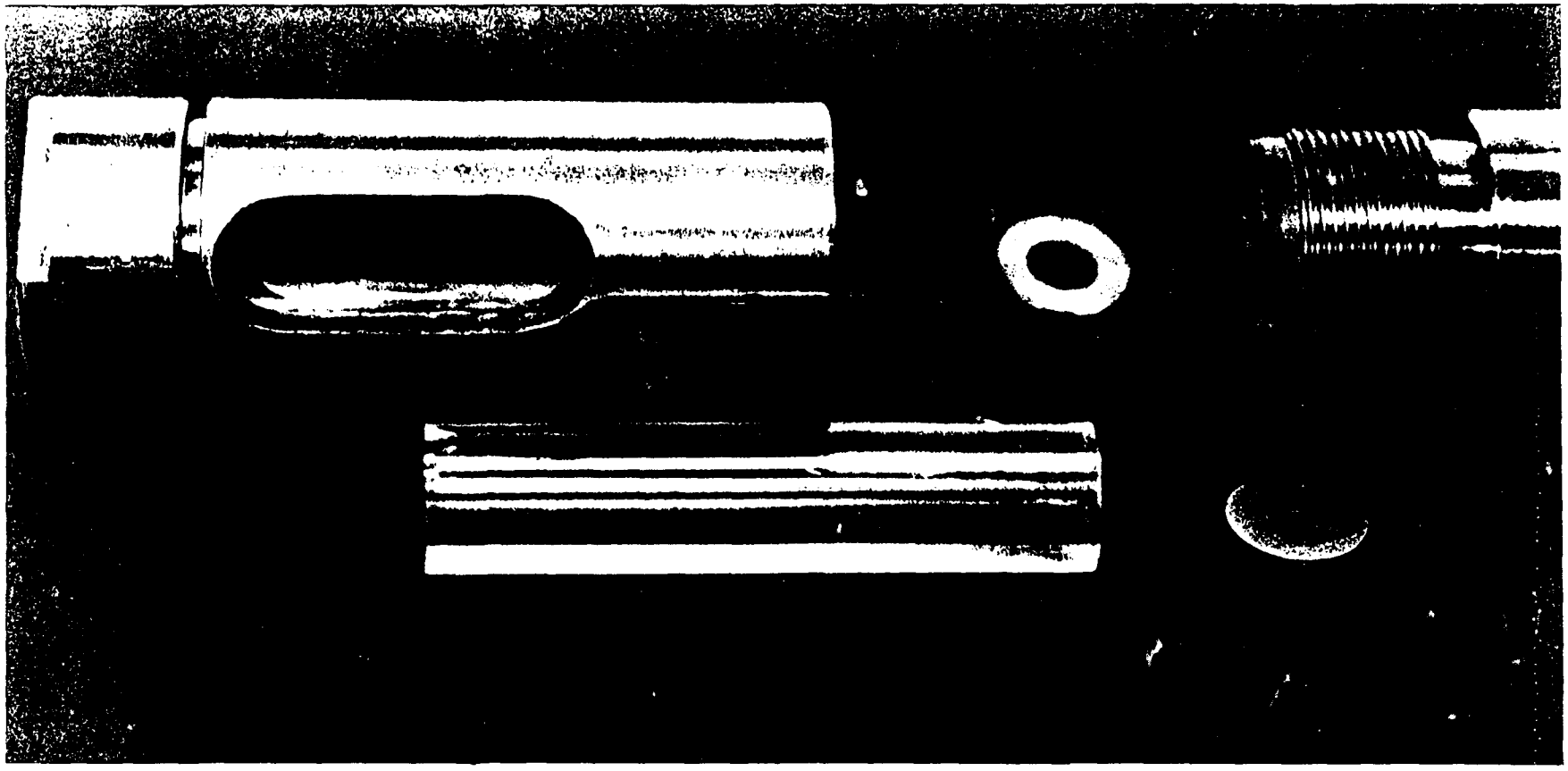

Figure 3.2 - Capillary components.

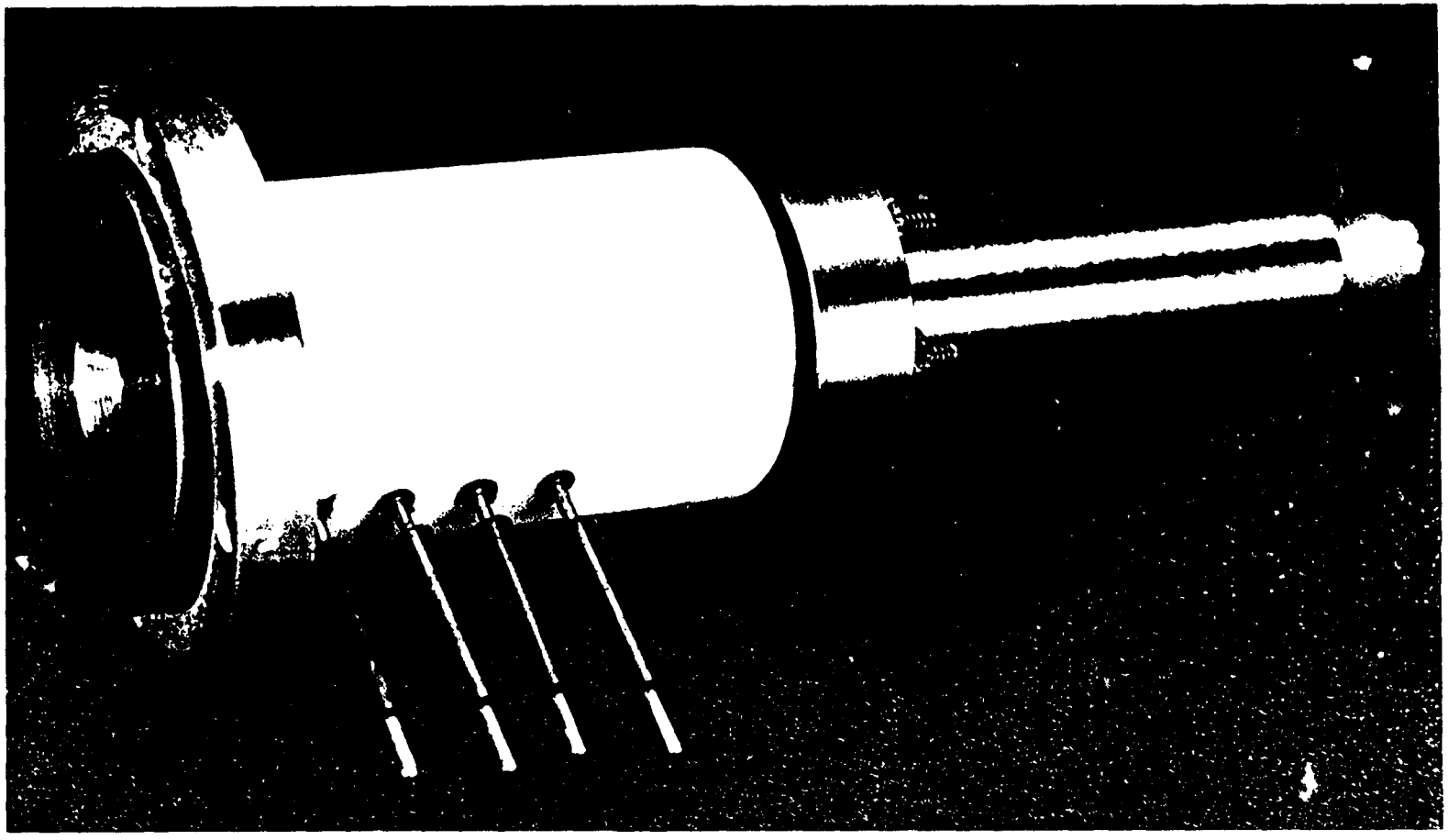

Figure 3.3 - Maycor capillary structure with voltage monitoring pins spaced along the discharge length.

that no attempt was made to match the discharge energy to the available water, as would be desireable for efficient fuel utilization in thruster applications. Only a small fraction of the resident water mass is vaporized during the discharge time (1-30 % depending on energy and injection conditions). Effects due to fuel depletion are not expected to be observed.

3.3 Discharge Circuit

A schematic of the circuit is shown in Fig. 3.4. The PFN was composed of identical LC stages with an impedance of 0.38 Ω. Pulses of 15, 30, and 60 μs nominal width were obtained for N = 3, 8, and 17 stages respectively. Initial tests, using only 3 stages, gave a limited view of the discharge dynamics. Most of the data was obtained with a 30 μs pulse. A few experiments to examine the approach to steady state were run with a 60 μs pulse.

The resistor R_D in series with the capillary was used as a load matching element. Since the capillary resistance was generally in the range of 100-250 mΩ, R_D helps to damp oscillations. At the same time, R_D acts as a buffer in that the time dependence of the driving current is relatively independent of the capillary resistance.

3.4 Optical System

The experiment was basically a table top one (Fig. 3.5). The capillary inserts into a small vacuum tank with optical access windows. A fiberoptic pickup and broadband photodiode provided routine monitoring of amplitudes and timing of the plasma emissions.

The major instrumention for spectroscopic work was an EG&G PAR Model 1460 GID OMA III optical multichannel analyser system. The detector head, Model 1420, has a 700 channel silicon detector array with microchannel plate intensification. Optical response peaks near 400 nm and the minimum detectable signals are 5-10 photons per channel. The detector is gatable to 5 ns though these experiments used 200 ns gating which gave quite acceptable time resoluton and signal level. The spectrograph is an Instruments S.A., Inc., Model HR320 having F/5.4 and 0.32 meter focal length. Interchangeable low and high resolution gratings were purchased. Survey studies under low resolution (0.5 nm/channel) were made during the initial investigations. Higher resolution (0.06 nm/channel) was required to isolate the oxygen emission lines used for temperature measurements.

3.5 Experimental Matrix

Figure 3.6 shows the parameter domain that has been studied. The primary variables were water injection conditions and capillary bore diameter. The effects of power loading on a given configuration were obtained by simply varying the PFN charging voltage. The case of water wall injection into a small bore capillary was not examined. A brief series of shots were made without water injection. These "dry" discharges were intended to view the extent to which the liquid water is controlling the discharge dynamics.

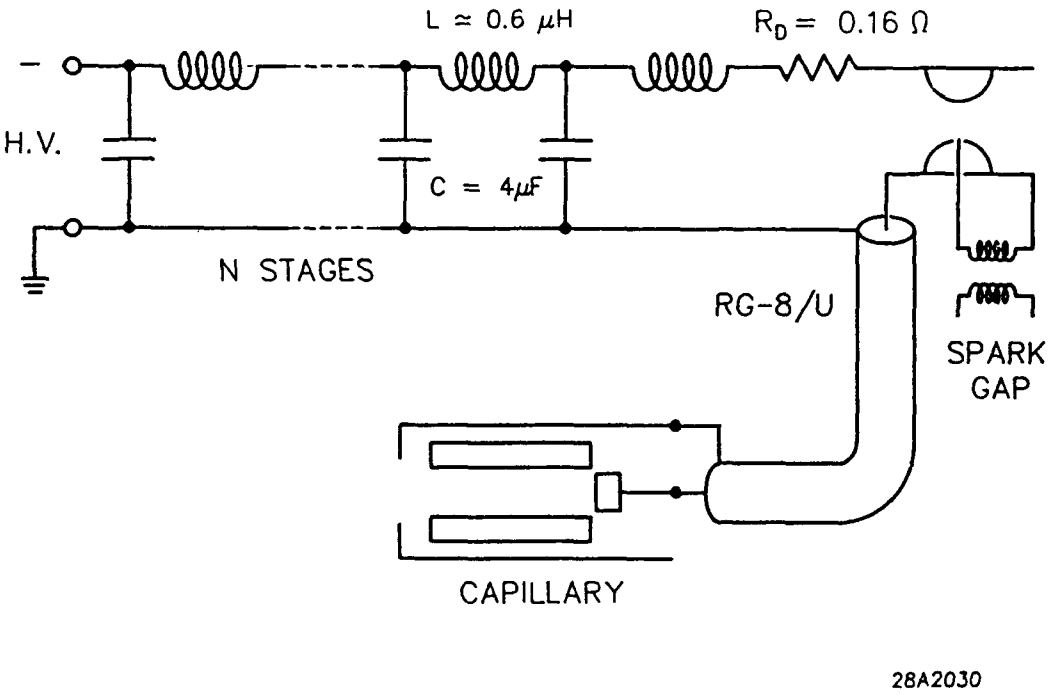

Figure 3.4 - Discharge schematic.

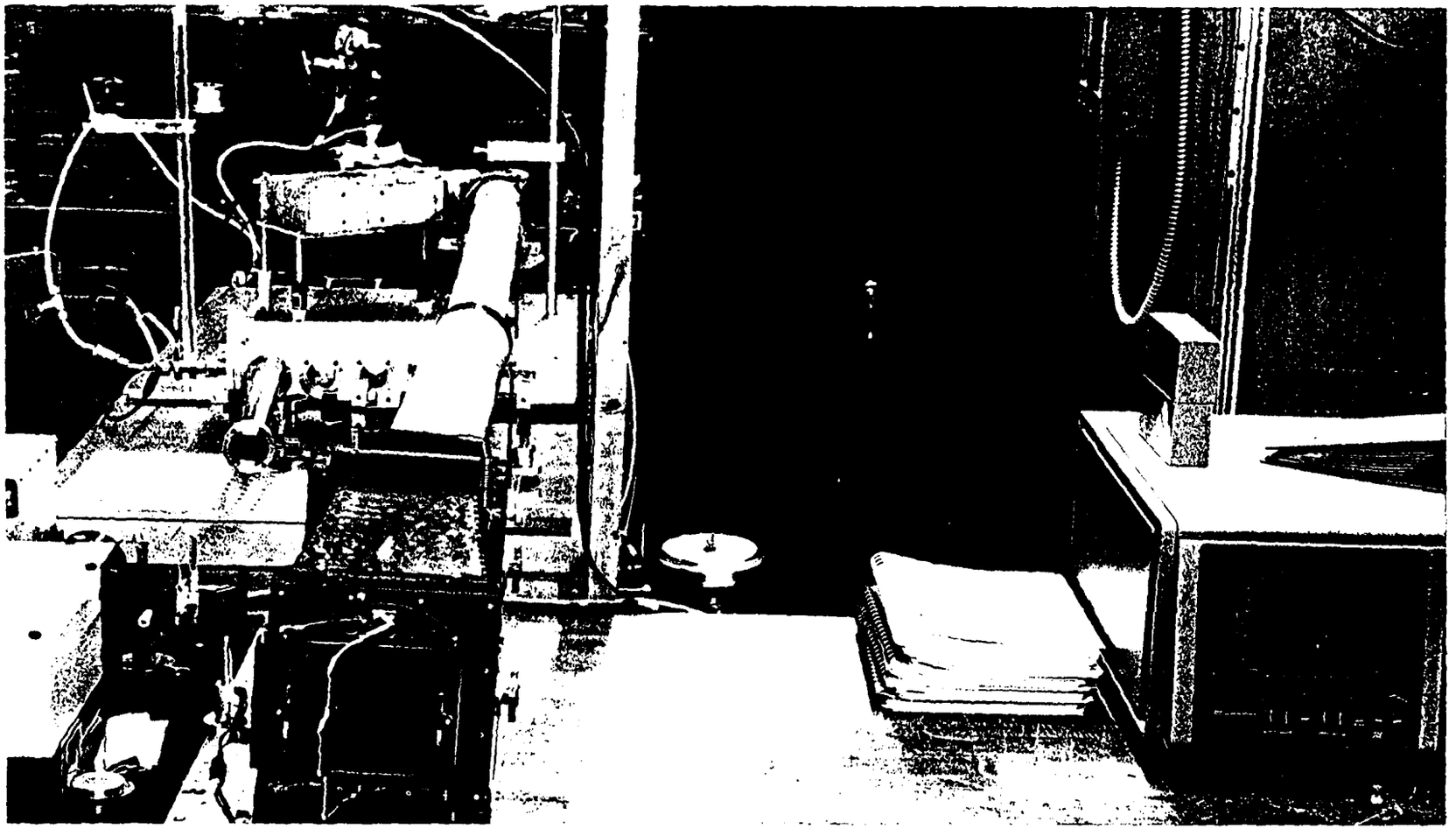

Figure 3.5 - Laboratory layout.

	WATER INJECTION		NO WATER INJECTION	
CAPILLARY DIAMETER	WATER WALL	STRAIGHT JET	POLY	QUARTZ
5 mm	3–4 kV	2.5–5 kV	3–4 kV	3–4 KV
3.5 mm		3–5 kV	3–4 kV	3–4 kV

Figure 3.6 - Matrix of experimental parameters studied.

4.0 RESISTANCE MEASUREMENTS

This section describes the results of a champaign to accurately measure resistance-time histories of the capillary under various discharge conditions. Previous short pulse experiments ($t \sim 15\ \mu s$) gave only a limited view of the discharge dynamics.[4] Pulses of 30 μs duration were used to obtain the majority of the data and these pulse widths reveal the full characteristics of the dynamic response. Steady state behavior is evident in the longer pulse ($t \sim 60\ \mu s$) data.

Resistance data was obtained as $R = V/I$ from the net voltage drop and the total current. In order to make very accurate measurements of resistance it was necessary to subtract out of the total voltage an inductive component which was due primarily to the inductance of the current feedthrough shaft ($L \sim 100$ nH). In most cases, especially at early times $t < 5\text{-}10\ \mu s$, the dynamic features were obscured unless careful attention was paid to extracting only the purely resistive component of the voltage drop.

4.1 Discharges Using Water Injection

The main parameters varied were: 1) water injection conditions, 2) capillary bore diameter, and 3) PFN charging voltage. The effects of these different conditions are discussed below while the data is summarized in Fig. 4.1. The data is presented as curve pairs corresponding to a low and high voltage discharge (solid and open circles for 3 kV and 4 kV charging voltages respectively). Each pair of curves represents a given injection condition and bore diameter. Current profiles for the discharges using water wall injection are included in Fig. 4.1 for reference.

A few general expectations are born out in this data. In all cases the initial breakdown ($t < 5\ \mu s$) and final cooling stages ($t > 25\ \mu s$) show a cool, high resistance plasma since the ohmic heating power is quite low. Comparing the small and large bore capillaries, an overall higher resistance results with the smaller bore. All else being equal, the resistance would scale simply with the cross-sectional area. In the two straight jet cases, the resistance might be expected to differ by approximately $(5.0/3.5)^2 = 2$, which is roughly as observed. Comparing different injection conditions (water wall vs straight jet in the 5 mm bore) a higher resistance for the water wall results due to the much larger surface area of water exposed to the plasma. An increase in water surface area would yield a higher flux of vapor resulting in a generally cooler, more resistive plasma. The two injection conditions in the 5 mm bore have surface areas differing by a factor of 25. The data in Fig. 4.1 does show a tendancy toward higher resistance with water wall injection though the sensitivity to surface area is rather weak.

Three distinct phases of the heating and vaporization dynamics are apparent during the flat top portion of the current pulse. Attention here is focussed on the straight jet data for the 3.5 mm bore capillary. The low resistance stage near $t = 5\ \mu s$ corresponds to heating and ionization of the background vapor only. (The ambient pressure in the vacuum chamber

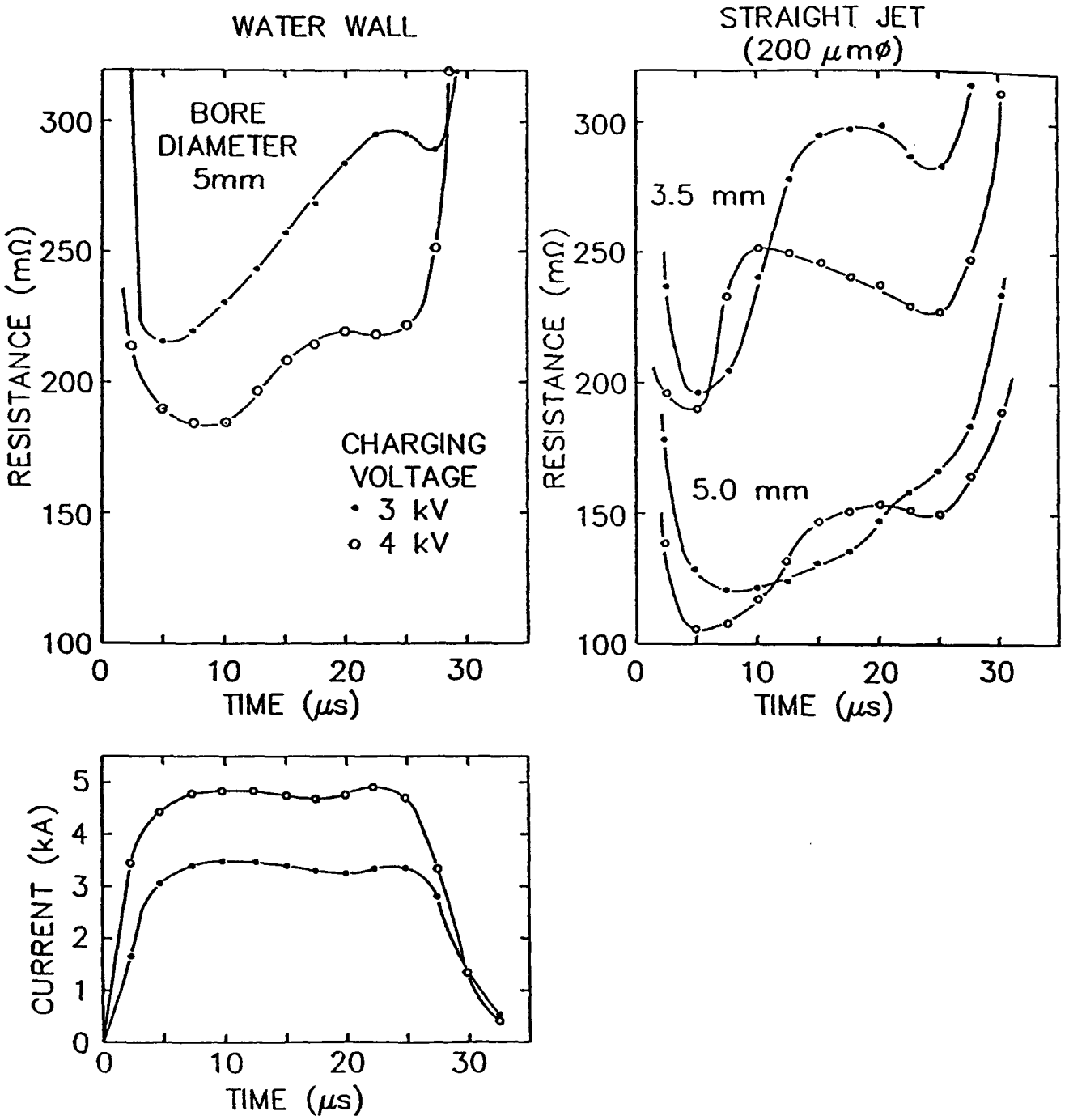

Figure 4.1 - Resistance data for various capillary configurations. The discharge current is shown for the cases having water wall injection.

was 4.5-5.0 torr water vapor.) A low gas density with high specific power density produces a fairly hot plasma. Measurements have shown that the plasma temperature is in excess of 3 eV during the initial heating phase. In the second phase the injected liquid begins to participate in the discharge. Water is ablated from the liquid surface to mix with and cool the plasma, resulting in an increasing resistance over times t ~ 5-15 μs. A third phase appears as the gradual drop in resistance over t ~ 15-25 μs. This resistance drop basically results from the increasing plasma density which manifests itself as a reduction of the $Z\ln\Lambda$ term in the resistivity.

Though the three phases noted above are most evident in the data for the straight jet with a 3.5 mm bore, all cases studied show the same basic trends. However, the timing and relative amplitude of the resistance modulations are quite sensitive to the various parameters surveyed.

A stable operating mode is not apparent in the data taken with a 30 μs pulse length. Shots taken with the longer 60 μs power pulse (Fig. 4.2) do show the development of quasi-steady behviour. The resistance reaches a steady value at about 20 μs for the 3.5 mm capillary and at about 30 μs for a 5 mm bore. A slight upward drift in resistance is seen after these times. Model results show the duration of the transient phase to be determined by the relaxation times for pressure and density.

It is worth pointing out that these experiments were not performed in a regime where the resident water mass was significantly depleted during the pulse time. If this were the case, one would expect a final transition to a high temperature, low resistance phase when the fuel is exhausted. Such studies would be a useful and important extension of the present work, particularly for those applications requiring efficient fuel utilization.

Axial variations in resistivity were evaluated using pin voltage measurements on the Maycor capillary (Fig. 3.3). Both the 5 mm and 3.5 mm bores were studied over a range of power levels. All cases had quite similar behavior with typical results shown in Fig. 4.3. The resistivity is very uniform along much of the capillary length and increases significantly near the anode where the exhaust plasma expands and cools. Gradients in the plasma parameters near the anode (notably temperature) will be much steeper than Fig. 4.3 indicates since the pin spacing allows only limited axial resolution.

4.2 Materials Comparisons

In an attempt to isolate the effects due to the water alone, additional resistance data was taken for discharges that did not have liquid water injection. Initial conditions of 4.5 torr background pressure were maintained by allowing a water vapor leak in the vacuum chamber. Two capillary materials were examined. The usual quartz tubes were used to see to what extent ablated wall material participates in the discharge. Other capillary tubes were constructed of high density, opaque (black) polyethylene. This would simulate the case of water wall injection conditions with a material that has identical surface area but is

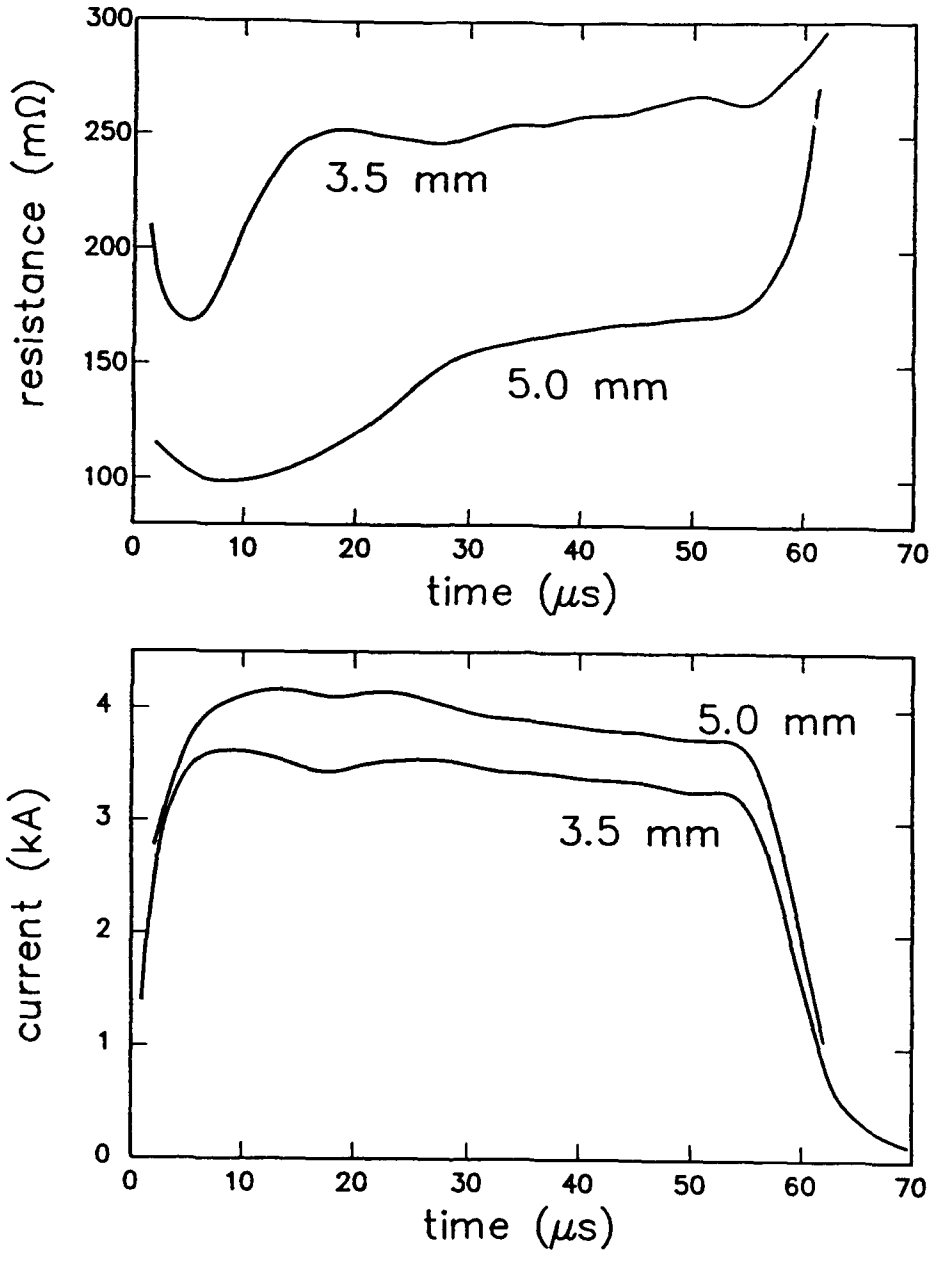

Figure 4.2 - Long pulse data for straight jet injection at 3 kV charging voltage.

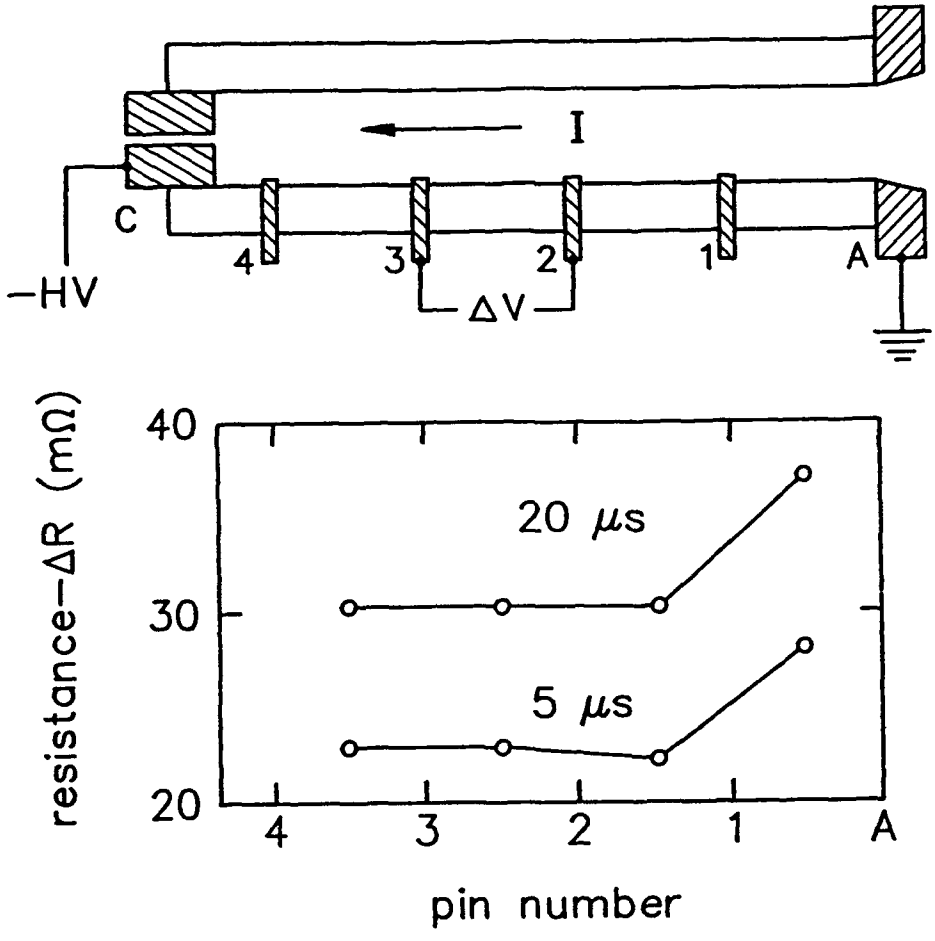

Figure 4.3 - Axial variation in resistance for a straight jet in a 5 mm bore capillary at 4 kV charging. The average resistance between pins is $\Delta R = \Delta V/I$. A resistivity of 2.1 mΩ-cm corresponds to ΔR = 10 mΩ.

somewhat less easily vaporized than water.

Figure 4.4 sumarizes the resistance data for these so-called "dry" discharges. Current traces for the shots using polyethylene are also shown in Fig. 4.4. The polyethylene data has the same generally slowly varying behavior as those cases with water wall injection conditions (Fig. 4.1), though the average resistance with polyethlyene is considerably lower. At a given power level, less mass is ablated from the polyethylene wall (compared with water) so that the discharge runs at a higher plasma temperature. The resistance for discharges in a dry quartz capillary show again the three phase structure. Several details of the resistance variations differ significantly from the corresponding data taken with water injection.

These "dry" discharges respond quite differently from those with water injection. The differences are ultimately tied to the basic thermal properties of the ablating material, i.e. thermal diffusivity, heat of vaporization, etc. For the purposes of this investigation the dry discharges are only qualitatively considered. The important aspect is that the behavior observed with water injection can be taken to be due primarily to the presence of the water itself.

The resistance measurement campaign has given a large body of accurate data on the discharge behavior. The goal of this research is to obtain a detailed understanding of the discharge dynamics displayed in Figs. 4.1, 4.2 and 4.3.

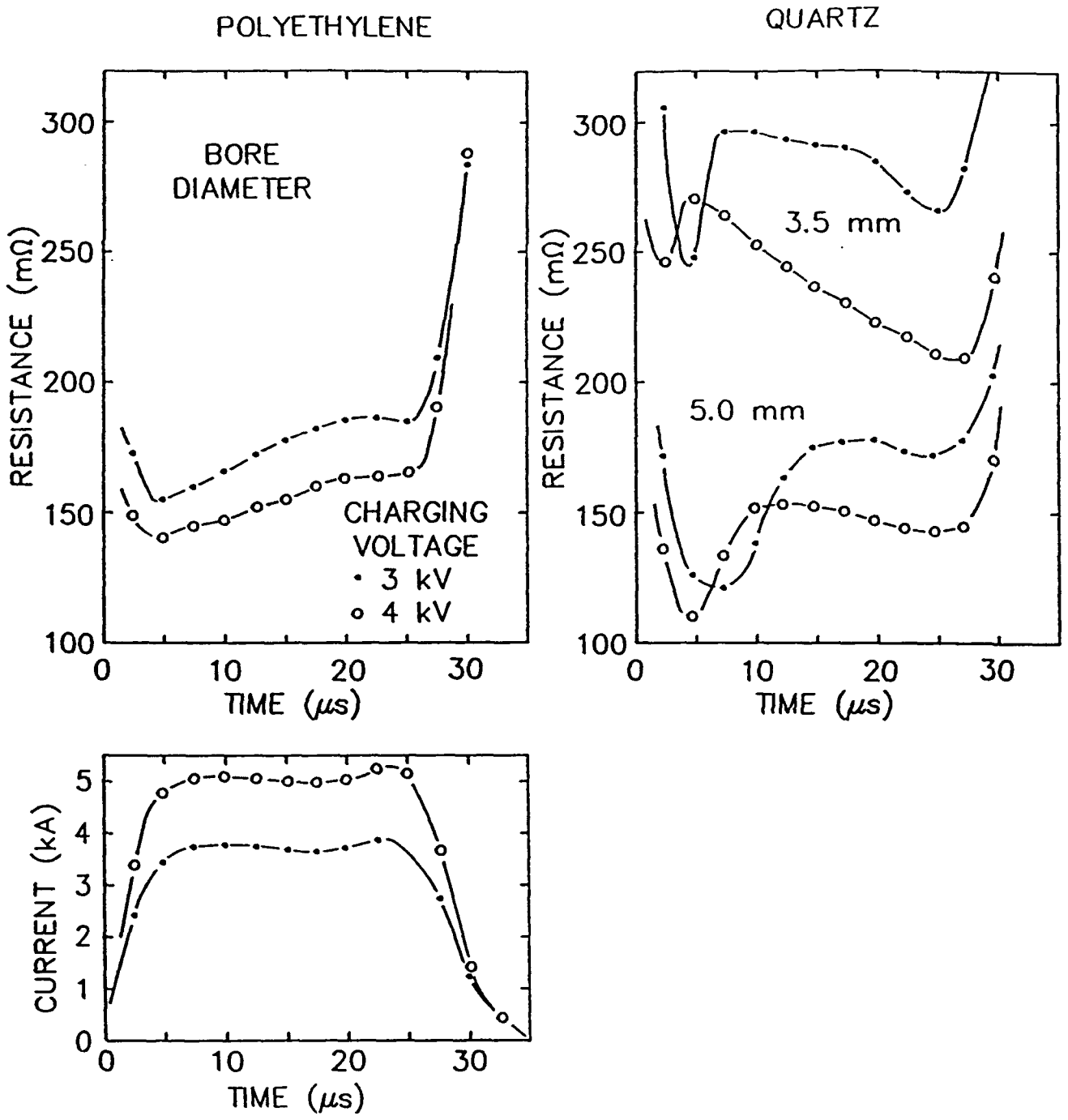

Figure 4.4 - Resistance measurements obtained using polyethylene and quartz capillaries. Liquid water was not injected into the discharge chamber.

28A-2-066

5.0 SPECTROCSOPIC STUDIES

Here we describe the optical studies that were made of the plasma emission. Broadband measurements made with a photodiode or with low resolution spectroscopy demonstrate the transition from optically thin to optically thick plasma conditions. Wall ablation is shown to severly limit optical access to the discharge. Where possible, detailed measurements of the plasma temperature have been made using the intensity ratio of oxygen emission lines. The temperature measurements have been restricted to times when the plasma is optically thin and sufficiently hot to have oxygen present in multiple stages of ionization. The data, though sparse, has been invaluable for understanding the role radiation plays in the discharge dynamics.

5.1 Broadband Response

A flavor for the kinds of low resolution spectra observed is given in Figs. 5.1 and 5.2. These were obtained using straight jet injection in a 5 mm bore capillary at a time of 14 μs into the discharge.

The spectrum in Fig. 5.1, taken with 3.8 kA peak current, shows an optically thin plasma radiating primarily through the hydrogen and ionized oxygen lines. Neutral oxygen does not appear since all the strong transitions in OI lie outside the visible region. The dense group of OII lines all originate from transitions with upper level exitation energies in the range of 25-30 eV. Under equilibrium conditions these high lying levels require $T > 2$ eV to have significant population densities. Silicon originates from the quartz wall and begins to show up in the spectrum when wall ablation sets in.[6]

In contrast to Fig. 5.1, the spectrum of Fig. 5.2 is seen with the discharge current at 5.5 kA giving approximately twice the average power input. Here the spectrum is almost completely dominated by silicon in the boundary layer of ablated wall material. In the warm inner regions of the boundary layer, singly ionized silicon is seen in emission. Cold regions close to the wall give rise to absorption in the resonant components of SiI at wavelengths of 265 nm and 300 nm. Under these conditions the opacity of the boundary layer prevents viewing plasma in the interior of the discharge.

In conjunction with the resistance measurements the temporal development of the plama radiation level was monitored via plastic optical fiber routed to a silicon photodiode. The fiber plus photodiode combination has a relatively broadband response so that signal levels will be indicative of the total radiation flux environment in the discharge chamber.

Radiation levels for a 5 mm capillary with straight jet injection are shown in Fig. 5.3 for three seperate charging voltages. Overlaying the traces on a single record with fixed sensitivity settings emphasizes the relative amplitude and timing of the radiation flux with respect to power input. These cases involve an optically thin plasma where radiation levels scale like the square of the plasma density. At early times the radiation from the background

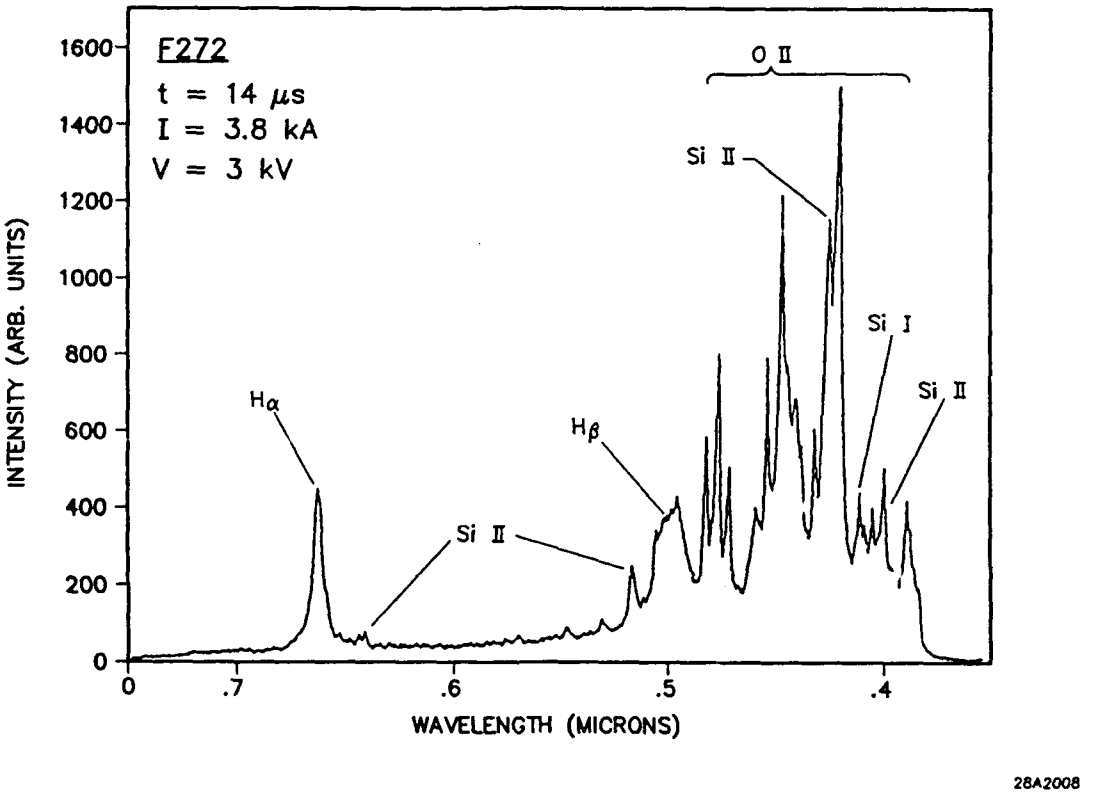

Figure 5.1 - Low resolution spectrum observed at t = 14 μs with straight jet injection and 3 kV charging.

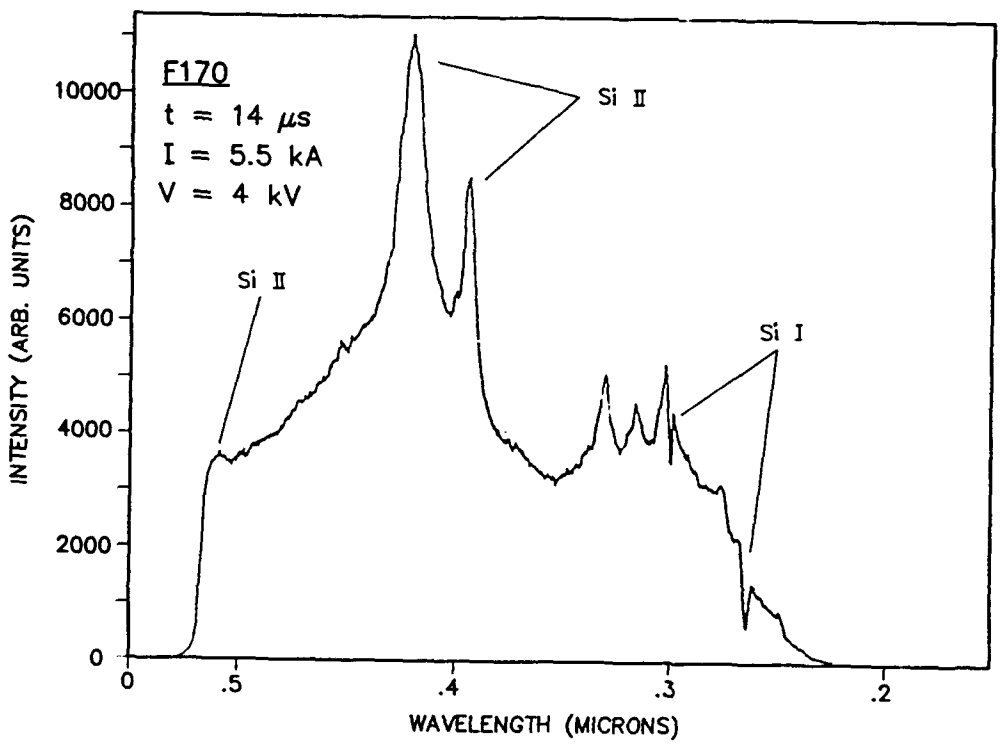

Figure 5.2 - Spectrum at t = 14 μs with 4 kV charging. The wavelength scale overlaps with Fig. 5.1 between 400-500 nm.

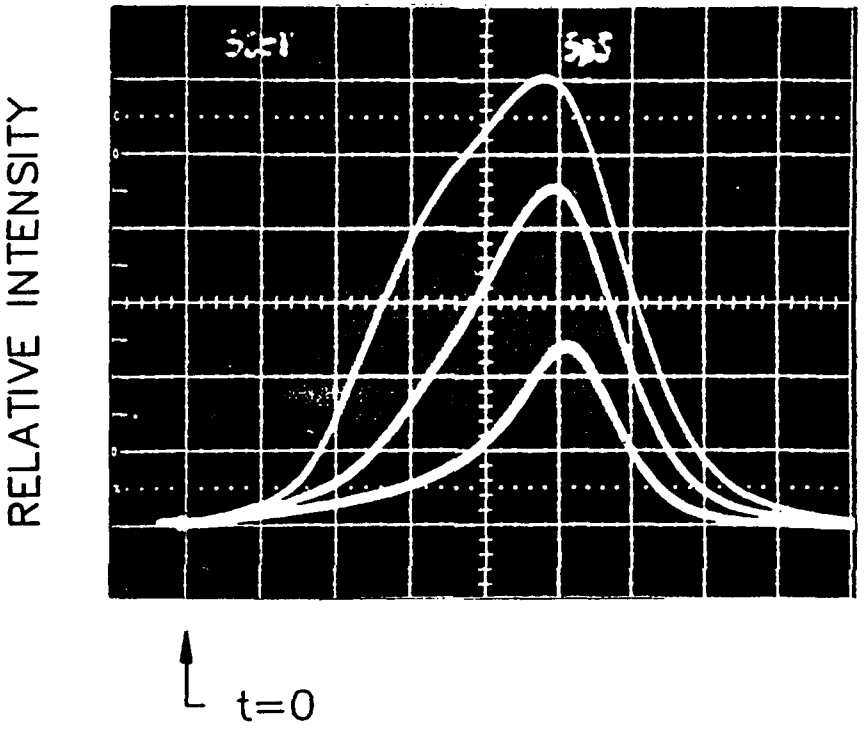

Figure 5.3 - Photodiode traces of the plasma emission levels for discharges using straight jet injection in a 5 mm bore capillary. Charging voltages were 3.0 kV, 3.5 kV, and 4.0 kV (lower to upper traces respectively). Time sweep is 5μs/div.

vapor alone is rather low. As vaporization of the liquid sets in the plasma density and radiative output increases significantly. Vapor generation cools the plasma with an attendant increase in resistance (Fig. 4.1).

The correspondence between radiation and discharge dynamics is best seen by comparing the photodiode signals (Fig. 5.4) and resistance (Fig. 4.1) for the 3.5 mm capillary. The first 5 μs has very small radiation levels during the low resistance phase. The radiation level then increases sharply and the timing of this increase is well syncronized with the resistance rise. Subsequently the radiation intensity appears to saturate near some maximum level. Additionally, the 4 kV shot in Fig. 5.4 shows a strongly decreasing intensity after the peak is reached. Two effects are being observed here. Firstly, the plasma transitions from optically thin to optically thick at which point the radiation intensity is indicative of the plasma temperature ($I \propto \sigma T^4$). This transition has been observed in similarly confined discharges.[7] Secondly, at high input power, wall ablation is severe and strong temperature gradients develop at the wall. Then, radiative losses occur through the outer regions of the boundary layer where the temperature and therefore radiation intensity is lower.

5.2 Temperature Measurements

This section gives some idea of the plasma temperature being observed in these discharges. Temperature diagnostics based on the absolute or relative intensities of spectral emission lines are well known techniques.[8,9] Application of these methods to the capillary discharge has been investigated using the available lines of hydrogen and oxygen. The usefulness of these methods has, however, been limited to early times when optically thin conditions prevail. Some success has been obtained using the intensity ratio of transitions from subsequent ionization stages of atomic oxygen.

The general expression for the intensity ratio of lines from an optically thin LTE plasma at temperature T is

$$\frac{I^z}{I^{z-1}} = \left(\frac{\lambda_{z-1}}{\lambda_z}\right)^3 \frac{g_{ik}^z f_{ik}^z}{g_i^{z-1} f_{ik}^{z-1}} \frac{2}{N_e} \left(\frac{2\pi mkT}{h^2}\right)^{3/2} \exp(-\Delta E/kT) \,, \tag{5.1}$$

where

$$\Delta E = E_k^z - E_k^{z-1} + E_\infty^{z-1} - \Delta E_\infty^{z-1} \,. \tag{5.2}$$

Here, z denotes the ion charge with z = 1 for singly ionized atoms. Transitions of wavelength λ originate from upper level k having exitation energy E_k. The lower level

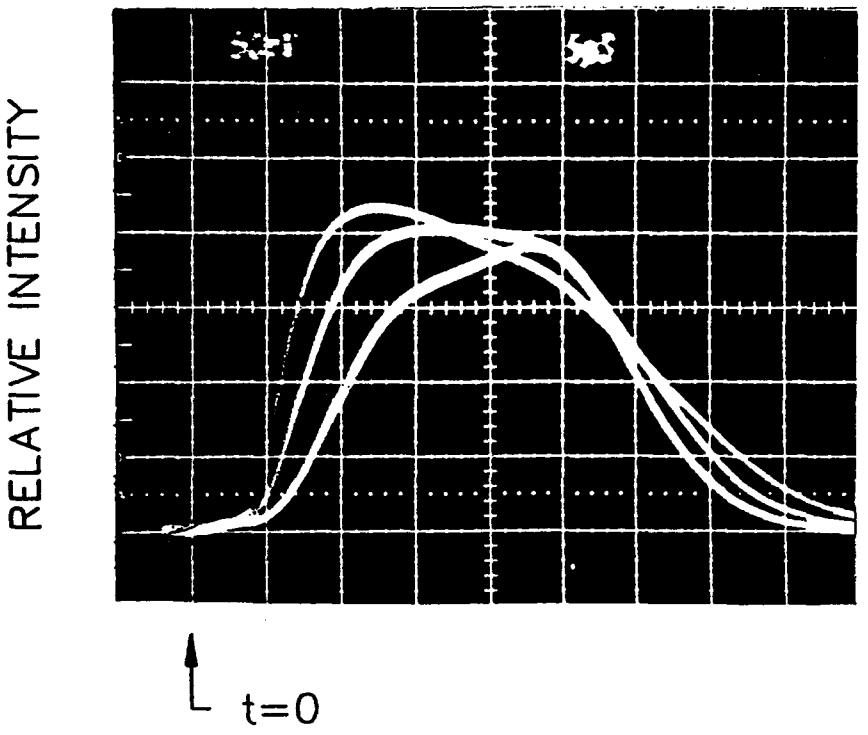

Figure 5.4 - Photodiode traces of the plasma emission levels in a 3.5 mm bore capillary. Charging voltages were 3.0 kV, 3.5 kV, and 4.0 kV. Time sweep is 5μs/div.

degeneracies g_i and absorption oscillator strengths f_{ik} are obtained from the NBS compilations.[10] The electron density N_e enters Eq. 5.1 through the Saha condition relating the relative abundance of the charged species. At high densities, the ionization energy, E_∞, may be reduced by ΔE_∞ due to Debye shielding or proximity effects.[11]

Several candidate transitions in OIII and OII were observed. Figure 5.5 shows a 10 nm band of the emission spectrum centered about the prominent OIII lines: The spectrum was obtained in a non-imaging arrangement and as such represents a spatially averaged profile. The diagnostic lines used were from OIII at a wavelength of 375.987 nm and from OII at 374.949 nm. Table 5.1 gives the relevant atomic data for these transitions. The OIII transition given in Table 5.1 was the strongest of those observed for doubly ionized oxygen. The proximity of a suitably strong OII line is convenient since the spectral sensitivity of the detection system can be assumed equal for both lines.

Table 5.1 - Atomic parameters for the diagnostic lines.

Species	λ (nm)	E_∞ (eV)	E_k (eV)	$g_i f_{ik}$
OIII	375.987	54.93	36.48	1.59
OII	374.949	35.15	26.30	0.76

Evaluating Eqs. 5.1 and 5.2 for the diagnostic lines chosen gives

$$\frac{I(OIII)}{I(OII)} = \frac{6.25 \times 10^{23}}{N_e} \left(\frac{T}{13.61}\right)^{3/2} \exp(-45.33/T) , \qquad (5.3)$$

where the plasma temperature and electron density have units eV and cm^{-3} respectively. Lowering of the ionization potential has been neglected. Though ΔE_∞ can amount to 1-2 ev for these capillary discharges, the essential results are not seriously effected by this simplification. Plots of Eq. 5.3 are shown as the solid lines in Fig. 5.6. The intensity ratio is seen to be strongly depenent on temperature and relatively insensitive to electron density. These features make the line ratio approach generally quite attractive for diagnostic purposes, provided suitable emission lines can be found. Signal to noise levels limited the range of detectable intensity ratios to about $20^{\pm 1}$ so that only temperatures in the range of 2.5-4.5 eV could be reliably measured.

Experimental values for the line ratios and corresponding plasma temperatures are also plotted in Fig. 5.6. The data shown was obtained for a 3 kV shot in a 5 mm bore

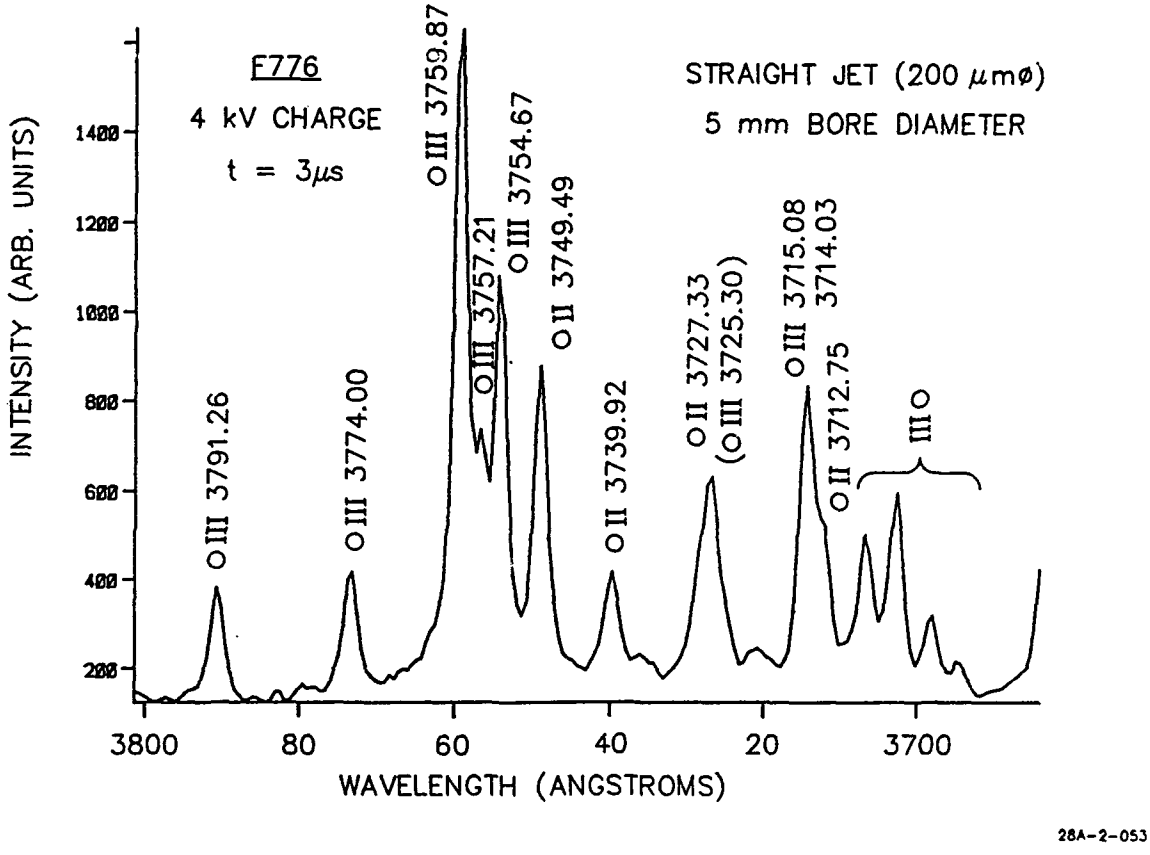

Figure 5.5 - Sample spectrum of oxygen transitions observed at early times in the discharge.

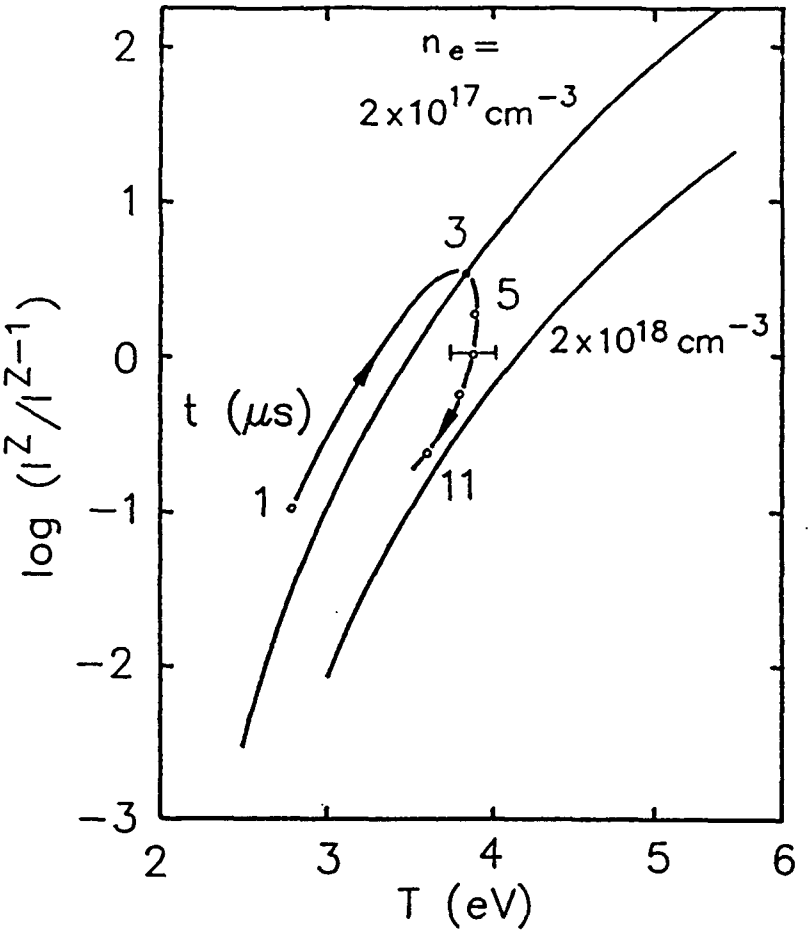

Figure 5.6 - Solid lines plot the theoretical intensity ratio of the OIII and OII diagnostic lines. The data points show experimental values for a 5 mm capillary at 3 kV using straight jet injection.

capillary under straight jet injection conditions. In this case, the OIII lines are detectable for up to 11 μs into the discharge (Fig. 5.7). Electron densities used in Eq. 5.3 were taken from previous measurements of Stark broadening in the hydrogen lines H_α and H_β under similar discharge conditions.[4]

The most obvious errors entering to the evaluation of temperature would be as follows. Line intensities can be measured with quite reasonable accuracies (±10 %). The error bars indicated Fig. 5.6 correspond to an uncertainty of ±50 % in N_e or, equivalently, an uncertainty in ΔE_∞ of ±2 eV. Additional errors are introduced through the transition probabilities which are considered accurate to ±25 %. Nevertheless, the line ratio method is sufficiently immune to the above uncertanties that the basic result is unchanged, namely, the plasma temperature at early times is in the vicinity of 3.5-4.0 eV.

5.3 Survey Spectra

The example in the previous section of using the OIII/OII line ratio approach to temperature determination is not fully representative of the observations that have been made. This section gives a brief survey of other discharge conditions and, in particular, emphasizes some of the general problems encountered in spectroscopic measurements on these discharges.

Figure 5.8 presents the temporal behavior of the plasma emission spectra over a 40 nm band centered on the OIII/OII diagnostic lines. In the discharge using a 5 mm bore with water wall injection, OIII is not detected beyond t = 5 μs and the spectrum shows only continuum emission for t > 8 μs. This sequence demonstrates that discharges using water wall injection cool quite rapidly once vaporization begins since there is a large surface area of water exposed to the plasma. The other sequence of shots in Fig. 5.8 is for an energetic discharge (4 kV) in a small bore capillary. Again, OIII is observed for only a few microseconds into the pulse. Strong emission from SiII appears for t > 4 μs due to severe ablation of the wall material (quartz). A cold, optically thick boundary layer quickly develops at the wall making it difficult to optically access the core plasma.

It is interesting to note the appearence of neutral silicon at t = 1 μs in the straight jet case of Fig. 5.8. The explanation for this is as follows. Initial breakdown of the background gas proceeds with the current confined to a hot filamentary arc. Typically, the current distribution spreads to fill the capillary bore on time scales of 2-5 μs.[12] High energy photons from the filament photoablate silicon from the wall. Neutral silicon lines are observed as the ejected atoms thermalize near the wall in the cold background gas. It is only after thermal ablation sets in that ionized silicon dominates the emission from the wall region.

A second observation concerning the initial breakdown process is that non-LTE

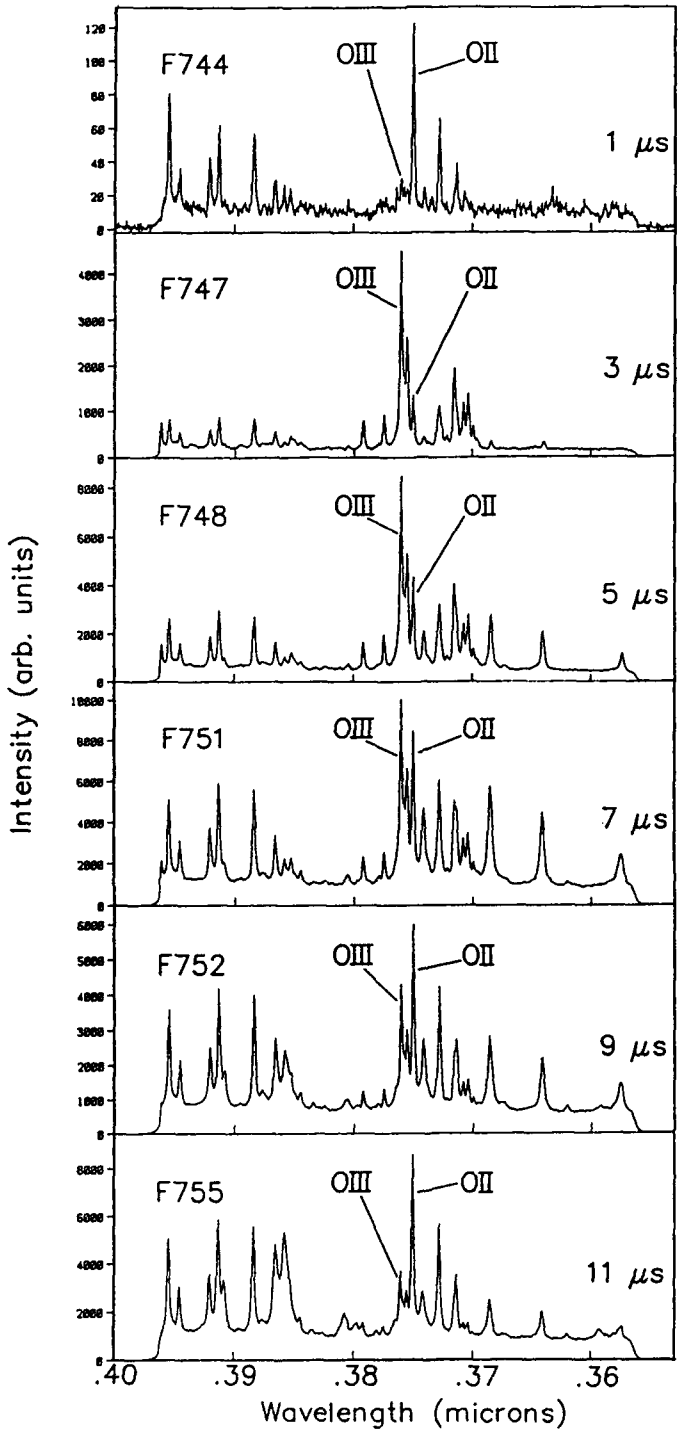

Figure 5.7 - Time scan of the oxygen line spectra used for temperature estimates in the 5 mm capillary.

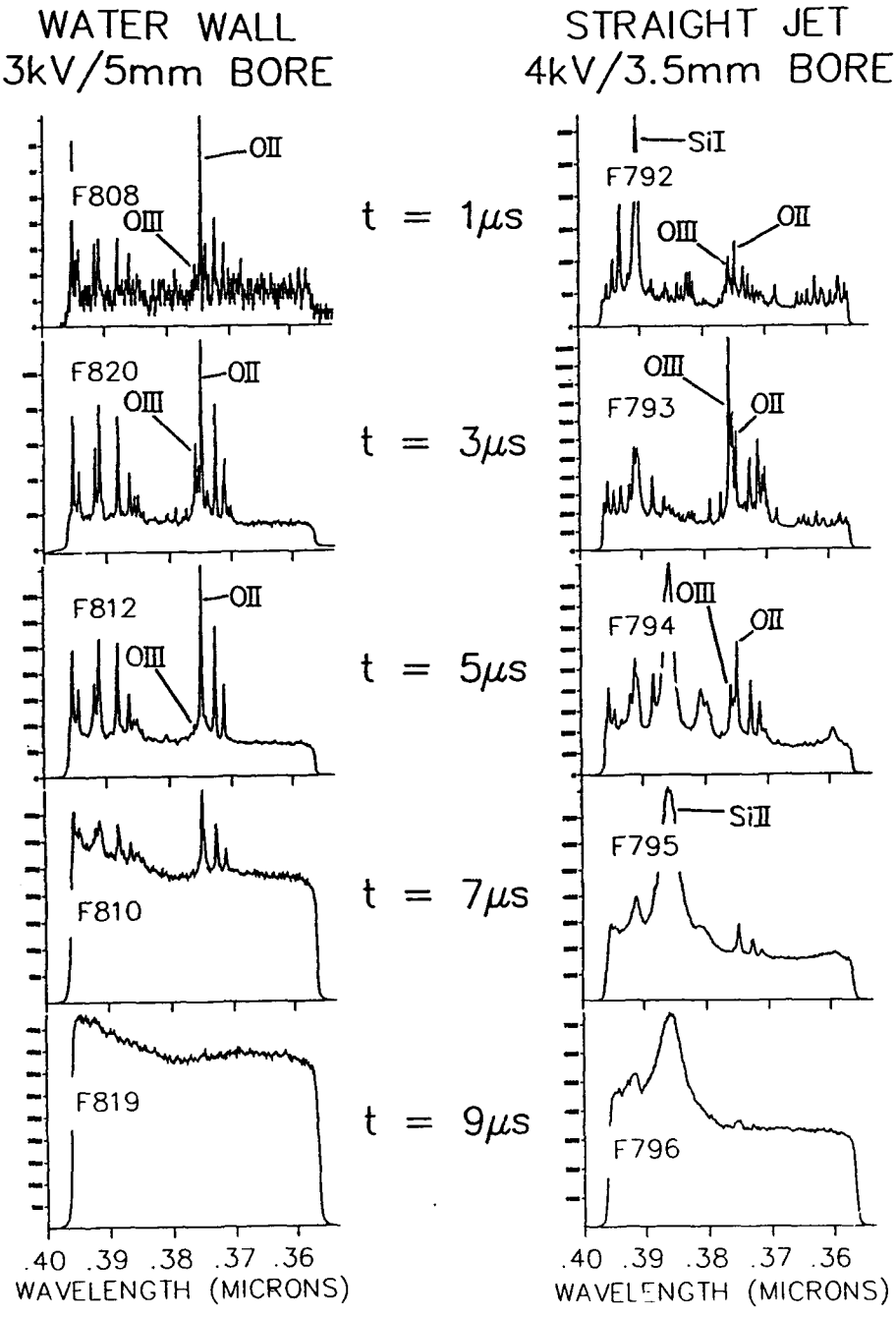

Figure 5.8 - Time histories of the plasma emission for different discharge conditions. Silicon from the wall and the oxygen diagnostic lines are indicated.

conditions can exist. Line ratio data for the higher energy shots show several OII transitions deviating significantly from calculated LTE intensities (Boltzman plots) indicating a coronal type equilibrium. Such deviations were only detected for $t < 2$ μs. Evaluation of LTE criterion has shown that, apart from the initial breakdown, LTE is maintained in these discharges.

In summary, the line ratio technique for temperature measurements has been successful up to times $t \sim 5\text{-}10$ μs. However, much of the interesting dynamics of the vaporization and mixing processes occurs at later times. Plasma cooling to the extent that OIII is not present and severe wall ablation have limited the usefulness of spectroscopic measurements for obtaining quantitative data on the discharge plasma.

6.0 DROPLET SHATTERING

The role of radial processes in determining the vaporization and mixing has been discussed previously.[4] The basic idea is that a high pressure, cold cloud of vapor may surround the liquid and expand into the hot plasma background with a speed ~150-300 m/s. Evidence for this has been suggested by a study of water droplet vaporization using CO_2 laser heating.[13] Alternatively, the liquid jet/droplets may breakup into a fine mist in the high velocity regions of the flow.[14,15] A brief series of experiments was performed to asses the presence of such a vapor cloud and examine the stability of the liquid in the fast axial flow field.

A nitrogen laser (150 mJ in a 3 ns pulse) was used for backlight photography of the water jet as it is exposed to the exhaust plasma. Direct photographic access to the capillary bore was not attempted. The shadow pictures in Fig. 6.1 were taken in the plasma flow a few millimeters outside the exhaust port. The photograph in Fig 6.1 at t = 10 μs is identical to the pre-discharge conditions. (Downstream of the injection orifice the straight jet pinches off into a steady stream of large droplets.) Some distortion of the droplets is seen around t = 20-30 μs, i.e., near the end of the power pulse. Eventually the droplets do shatter into a fine mist.

There does not appear to be any evidence of a dense vapor cloud surrounding the liquid. This suggests that the water evaporated from the liquid surface mixes rapidly with the flowing plasma. Though droplet breakup is occuring, it is unclear whether or not this is an *important effect inside the capillary for pulse times less than ~ 30 μs. In particular, such* breakup of the liquid would not be expected to occur near the cathode where the plasma flow velocity is small. However, liquid breakup may well be an important process in high power and/or long duration pulses.

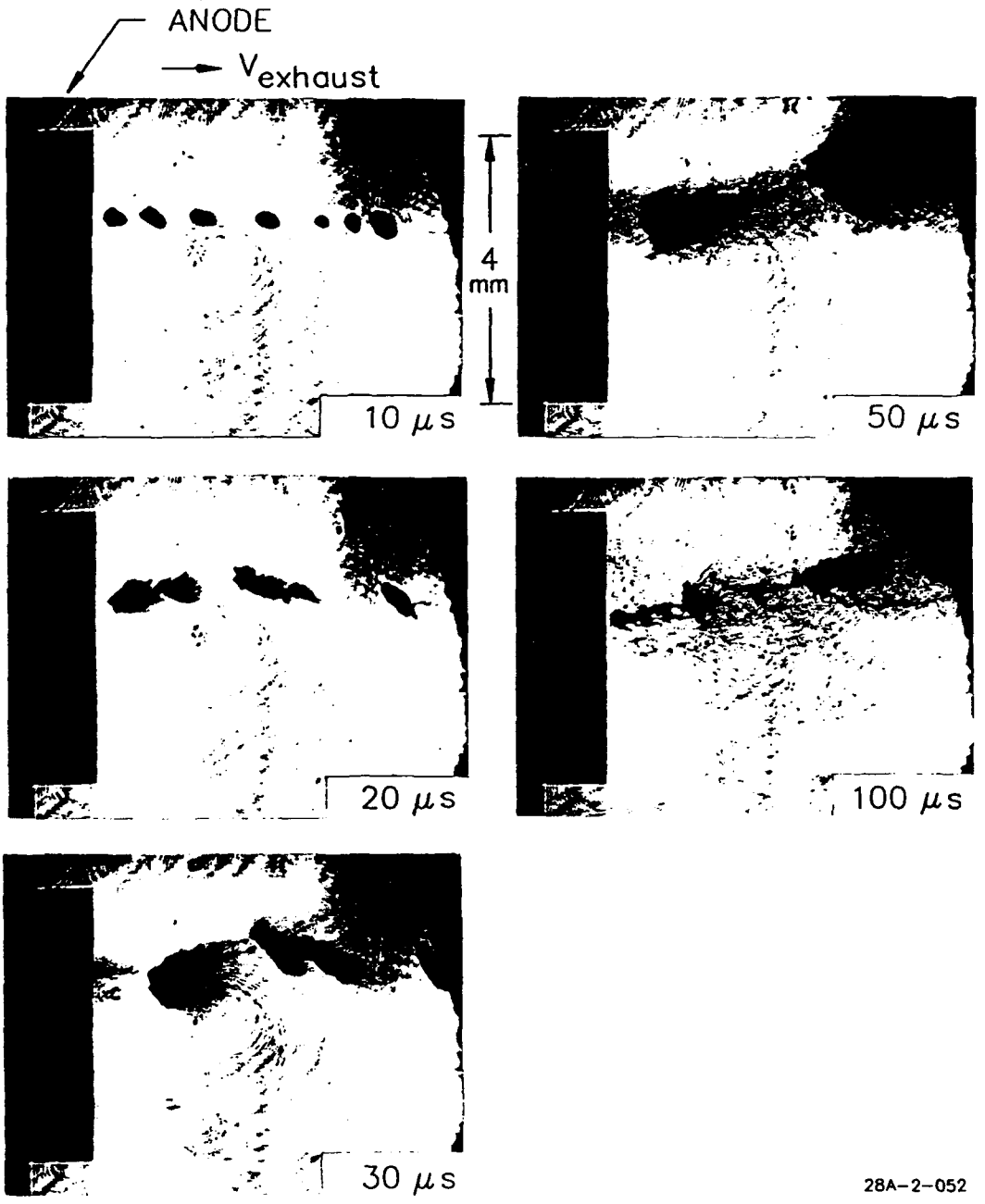

Figure 6.1 - Shadow photographs of the liquid jet exposed to the exhaust plasma. The discharge conditions were: straight jet injection, 3.5 mm bore capillary, and 3 kV charging.

7.0 NUMERICAL MODELING

This section describes our efforts to formulate a physics model of the discharge. Considerable theoretical work has been done to model the basic processes governing the behavior of high power, high pressure, ablating wall discharges.[16,17,18] The features of the model are outlined and specific adaptations for the present problem are described. Numerical solutions for several discharge configurations are provided and compared with the experimental measurements.

7.1 One Fluid, 1-D Model

The one dimensional conservation equations used to describe an ablation controlled capillary arc are

$$\frac{\partial \rho}{\partial t} + \nabla \rho v = \dot{\rho}_l \,, \tag{7.1}$$

$$\frac{\partial \rho v}{\partial t} + \nabla(\rho v^2 + P) = 0 \,, \textit{ and} \tag{7.2}$$

$$\frac{\partial E}{\partial t} + \nabla v(E + P) = \eta j^2 - \frac{f Q_w}{\pi a^2} - \frac{1}{2}\dot{\rho}_l v^2 \,. \tag{7.3}$$

Equations 7.1-7.3 were derived[17] for the axial flow field in a cylindrical capillary tube of radius a.

Liquid injection is cylindrically symmetric and the liquid is assumed to occupy a negligible volume of the capillary. A straight jet has radius r, while the case of water wall injection is obtained by letting r = a.

The mass density introduced into the plasma flow due to vaporization of the liquid is

$$\dot{\rho}_l = \frac{Q_l}{\pi a^2 h} \,.$$

Heat transport from the plasma is $Q_l = 2\pi rq$ (W/m) where the liquid surface recieves a heat flux q (w/m^2) that is determined by the local plasma conditions. Energy lost to the liquid is returned to the plasma as ablated mass at the local specific enthalpy h (J/kg) of the plasma.

The model is essentially a one fluid (plasma) model. Vapor is not explicitly treated as a separate component of the flow since the ablated mass is assumed to be radially distributed instantaneously and uniformly across the capillary cross-section. Heat transport and ablation processes are taken to occur at the liquid surface in a thin boundary layer of negligable thickness.

Ohmic heating is the sole energy source and the current density is taken to be uniform across the capillary radius. Equation 7.3 includes the energy losses to the wall via the flux $Q_w = 2\pi aq$. For straight jet injection the jet surface area is a factor of 25 smaller than that of the wall so that wall losses are severe. Even in the case of water wall injection, a significant amount of radiation is transmitted through the wall. All calculations have assumed the maximum wall losses, f = 1. The final term in Eq. 7.3 describes frictional sweep-up of the source mass. The idea is that evaporated material passes from the liquid to the plasma through a thermal skin (boundary layer) and, in the process, aquires its axial velocity at the expense of flow energy.

Heat flux to the wall and liquid can arise from several sources such as conduction, radiation, and convective transport. Radiation tends to dominate with the flux usually taken at the blackbody limit $q = \sigma T^4$. However, these discharges are optically thin early in the pulse. A detailed treatment of radiation transport is a complex and time consuming calculation. Instead, an empirical approach was taken where a modified blackbody function describes the heat flux, i.e.

$$q = A(t)\sigma T^4 ,$$

and A(t) has the form

$$A(t) = \frac{1}{2}\left[1 + \tanh\left(\frac{t-t_0}{\tau}\right)\right] .$$

An explicit time dependence through A(t) is intended to roughly simulate an optically thin to thick transition. Radiation flux is suppressed at early times and passes into the blackbody limit near time t_0 at a rate determined by τ. Additionally, there remains the time dependence through the temperature T(t). This formulation of the heat flux was found essential to describing the early time history of the discharge.

The analytic function A(t) was convenient for incorporating into the numerical calculations and easily obtained from the measured emission levels. The amplitude function was found in each case by fitting to the rising portion of the photodiode signals. For example, two cases modeled with straight jet at 3 kV were the 5 mm bore where $t_0 = 30\ \mu s$ and $\tau = 11\ \mu s$ (Fig. 5.3) and the 3.5 mm bore where $t_0 = 10.5\ \mu s$ and $\tau = 5.0\ \mu s$ (Fig. 5.4).

It has been equally important to have a description of the plasma resistivity that covers a broad range of conditions. Electron-neutral and Coulomb collisions are included by taking the resistivity as[19]

$$\eta = \eta_s \left(1 + \frac{2\nu_{eo}}{\nu_{ei}} \right) .$$

Electron-ion and electron-neutral collision frequencies are[20]

$$\nu_{ei} = 3.5 \times 10^{-6} \frac{N_e Z \ln\Lambda}{T^{3/2}} \quad s^{-1} \ , \ and$$

$$\nu_{eo} = N_o \sigma_{eo} \left(\frac{kT}{m_e} \right)^{1/2} \quad s^{-1} \ ,$$

where the electron and neutral particle number densities N_e and N_o are in cm^{-3} and the plasma temperature is in eV. The electron-neutral collision cross-section was given the value $\sigma_{eo} = 5 \times 10^{-15}\ cm^2$ as a reasonable approximation to the mean value for the hydrogen and oxygen species present.

The Spitzer resistivity is[21]

$$\eta_s = 3.04 \left(\frac{1}{\gamma_e} \right) \frac{Z \ln\Lambda}{T^{3/2}} \quad m\Omega - cm \ ,$$

with the Coulomb logarithim given by[20]

$$\ln\Lambda = 23 - \ln\left(Z N_e^{1/2} T^{3/2} \right) .$$

These expressions use the average ionic charge Z as defined in the appendix while the coefficient $1/\gamma_e$ is calculated from the equation

$$\frac{1}{\gamma_e} = 2.0783 - 0.4131Z + 0.0530Z^2$$

which interpolates between the values given in Ref. 20.

The system of equations is completed once the species concentrations and thermodynamic properties of the plasma are specified. This information was obtained by solving the Saha equations for an equilibrium water plasma. Full details of the composition calculations are given in the appendix. The total energy density (internal + kinetic) of the plasma is

$$E = W + \rho v^2/2 ,$$

while the internal energy density W and specific enthalpy are related to pressure through the enthalpy coefficient g in the usual manner, namely

$$W = \frac{P}{g-1} , \text{ and}$$

$$h = \frac{g}{g-1}\frac{P}{\rho} .$$

7.2 FCT Code

The numerical method used for this study is an algorithm developed specifically for the solution of time-dependent flow problems containing shocks or other steep gradients.[22] The FCT or Flux Corrected Transport algorithm incorporates methods of general applicability to accurately calculate the dynamics of a user defined set of fluid conservation equations. The computed results are corrected at each time step to remove the errors introduced by numerical diffusion. FCT can provide complete solutions to 2-D unsteady flow problems in the high density continuum regime and potentially can also model free

molecular flow.[23]

The capillary is modeled as a semi-infinite cylinder 80 mm long and divided into 200 uniformly spaced cells. Boundary conditions are zero flow velocity at one end (cell 0) and free flow through the other end. The discharge is confined to a 40 mm long section (cells 0-100) with the cathode at the closed end. This is the region of water injection and ohmic heating. The experimental current profiles were used as input to the code. Cells 101-200 form a drift section that has neither water nor electrical input. Wall losses were allowed throughout the entire computational domain. Initial conditions were set to the experimental values of 4 Torr ambient water vapor at 273 °K.

7.3 Steady State Time Scales

Initial code runs examined the general behavior of the capillary and the approach to steady state conditions using a very simpified model.[5] A step function current profile was used with an amplitude of 3.5 kA while the plasma resistance was held constant at 150 mΩ. The heat flux was taken always at the blackbody limit with no transitional time dependence (A(t) = 1) and no wall losses. An ideal gas having constant enthalpy coefficient g = 1.2 was assumed. The heavy particle density was $N = \rho/<A>m_p$ where m_p is the proton mass and the mean atomic weight for water is $<A> = 6$. In this case, ionization and electron pressure was not taken into account.

Figures 7.1 to 7.3 show the plasma flow velocity, pressure, and temperature throughout the computational domain at various times in the discharge for code run number CAP50. These calculations were made for a 5 mm diameter capillary with water wetted wall. A shock wave, seen near cell 195, is generated early in the discharge and propagates down the drift tube. The temperature profile remains particularly flat throughout much of the capillary length. Near the capillary exit plane (cell 100) the gradients steepen sharply. The flow is subsonic within the capillary and supersonic in the drift tube.

In principle one might expect steady state to be characterized by a relaxation time $t_r = 2L/c_s$ where L is the capillary length and c_s the plasma sound speed. The sound speed for water at 1 eV is $c_s \sim 4$ km/s making $t_r \sim 20$ μs. A relaxation time can be defined for the code runs as the time for a parameter to reach 80% of its steady state value. Table 7.1 lists these times for several of the fluid variables from the CAP50 calculation. It is noteworthy that the most responsive variable is temperature. Since the heat flux for ablation depends strongly on temperature, the dynamic response of the capillary will be most noticeable in temperature sensitive diagnostics such as the resistance measurements. Plasma pressure and density do respond on time scales comparable to t_s.

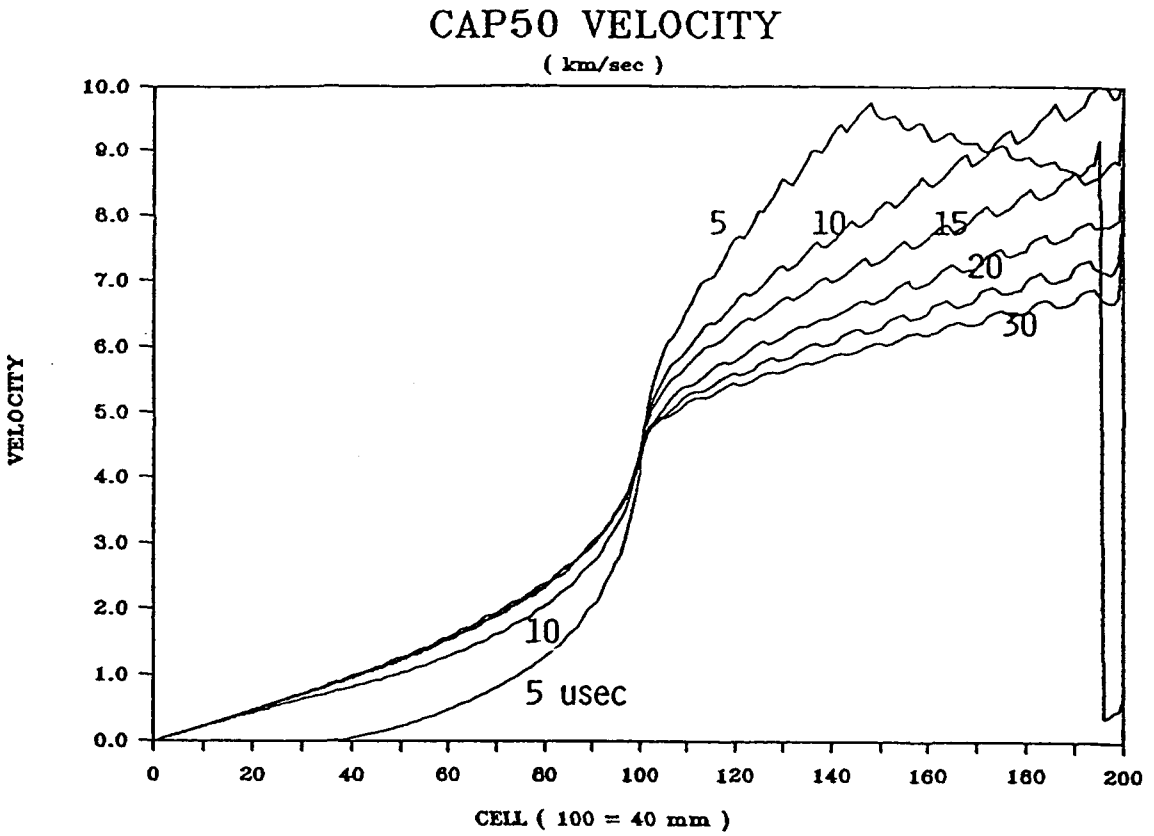

Figure 7.1 - Plasma flow velocity for CAP50 code run on a 5 mm capillary with water wall injection.

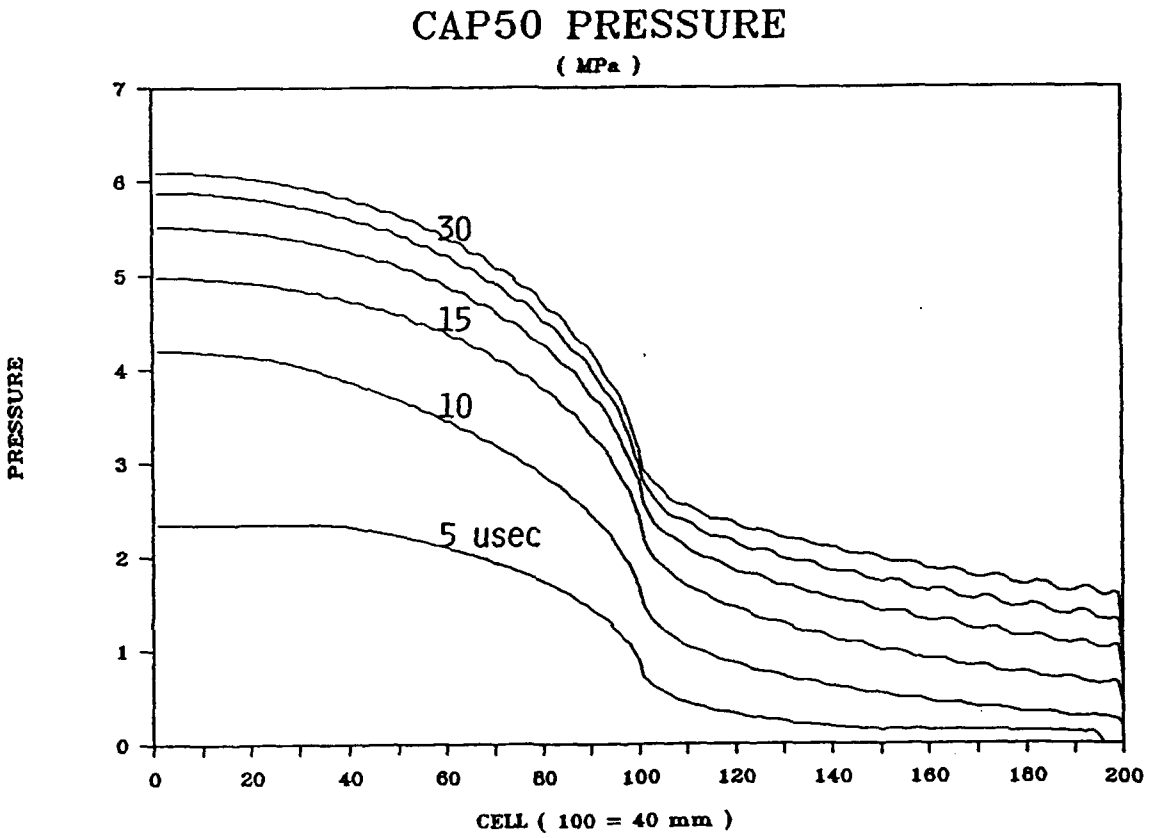

Figure 7.2 - Capillary pressure for CAP50 code run on a 5 mm capillary with water wall injection.

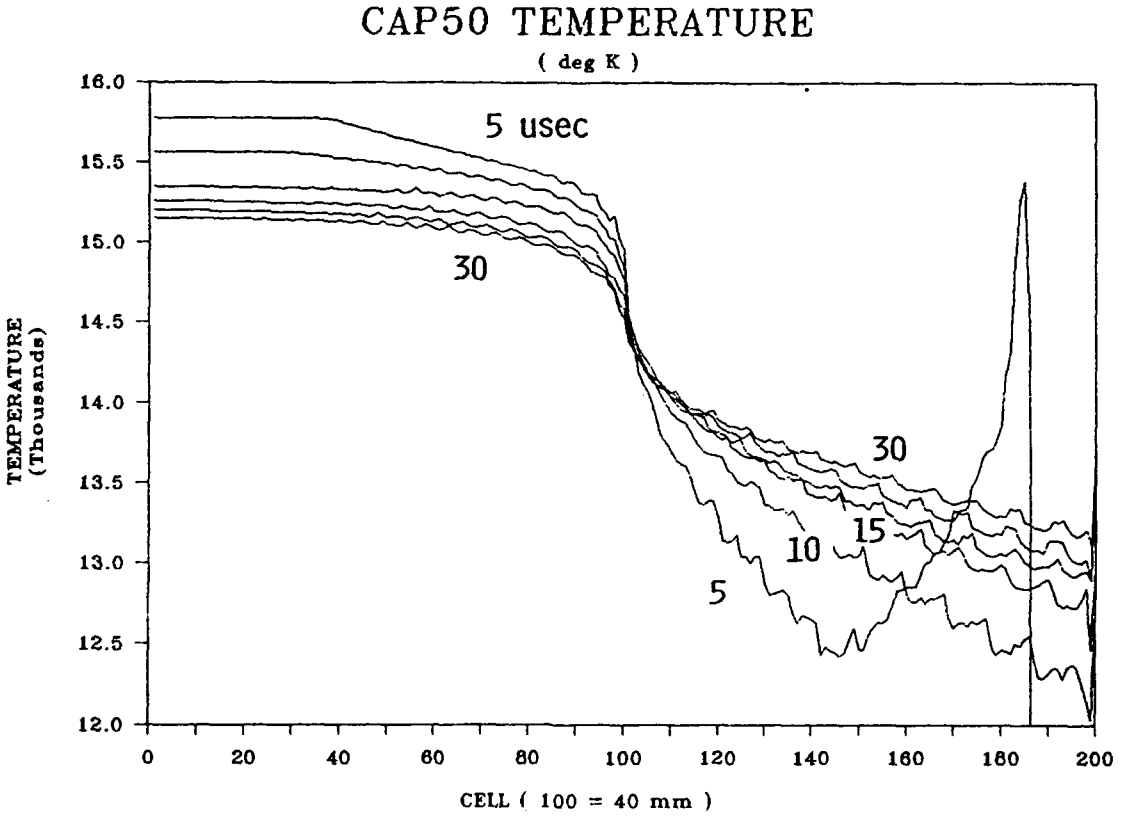

Figure 7.3 - Capillary temperature for CAP50 code run on a 5 mm capillary with water wall injection.

Table 7.1 - Relaxation times at the capillary midpoint (cell 50) for parameters of the CAP50 calculation.

Parameter	time (μs)
Current	0
Temperature	5
Velocity	20
Pressure	40
Density	40

7.4 Detailed Simulations

An extensive set of code runs was performed using the model as outlined in Sec. 7.1. Simulations were done for the complete experimental matrix using water injection (Fig. 3.6). This section presents the numerical results in detail for two cases roughly corresponding to the extremes of the range of discharge conditions covered in the experimental matrix. All simulations were for the 30 μs pulse experiments.

The first case (CAP83) is for water wall injection in a 5 mm capillary at 3 kV charging voltage. This represents the low temperature, high density, weakly ionized regime. Figures 7.4 - 7.6 show the spatial profiles of temperature, pressure, and flow velocity throughout the computational domain. Figures 7.7 - 7.9 give the time dependence of temperature, pressure, and density near the stagnation region (cell 2) at the cathode. Similarly, Figs. 7.10 - 7.15 give the corresponding data for straight jet injection in a 5 mm capillary at 3 kV representative of the hot, low density discharges.

In all cases, the temperature is very uniform within the capillary, while the gradients at the exit plane are much steeper than the data of Fig. 4.3 suggest. A somewhat unexpected result appears in the straight jet simulation near t = 5 μs where the density and pressure show a pronounced drop (Figs. 7.14 and 7.15). This drop is basically a "venting" of plasma that occurs as the flow velocity profile develops. Figure 7.12 shows the flow velocity at 5 μs beginning to increase near the cathode region (cell 2). Compare this with Fig. 7.6 for the water wall case where the velocity is zero throughout cells 0 - 35 at t = 5 μs. Such venting effects are pronounced only in the high temperature, high velocity cases where the velocity profile develops rapidly and there is insufficient time for vaporization to raise the density much beyond ambient (1.32×10^{-3} kg/m^3).

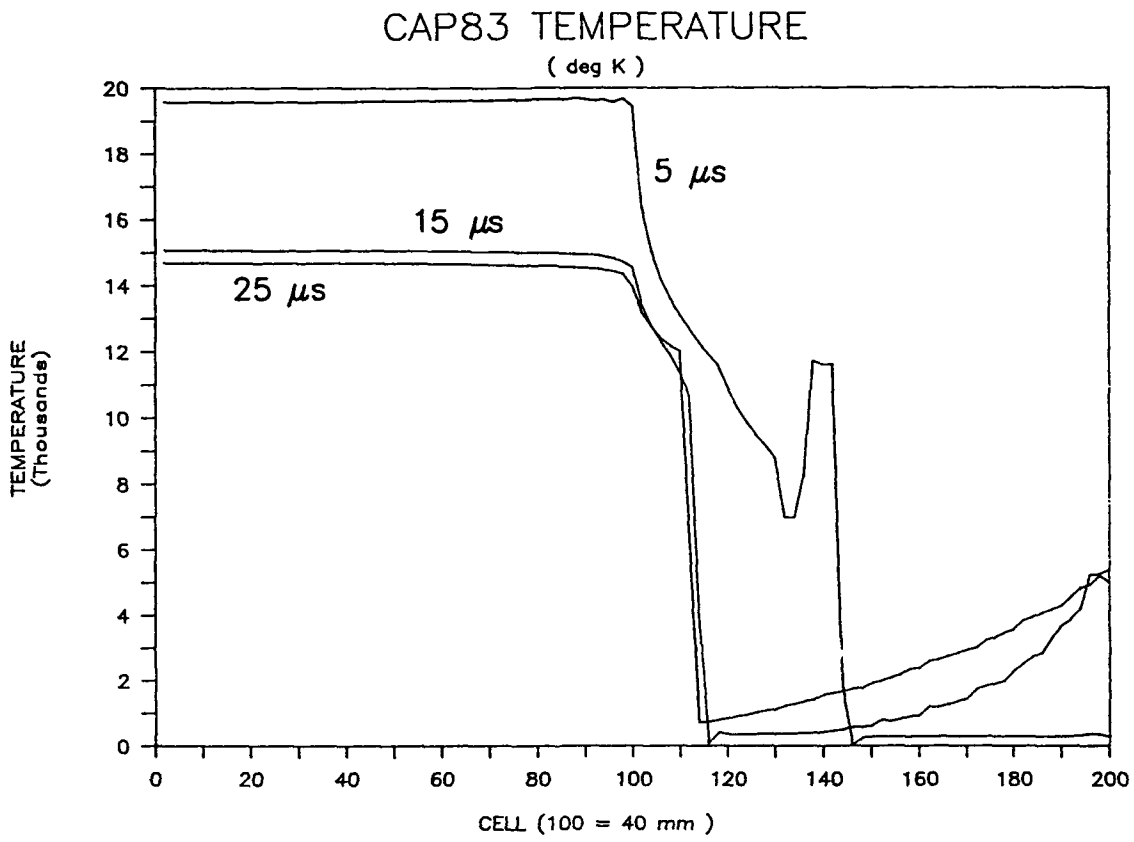

Figure 7.4 - Temperature profiles for water wall injection in a 5 mm capillary at 3 kV (CAP83).

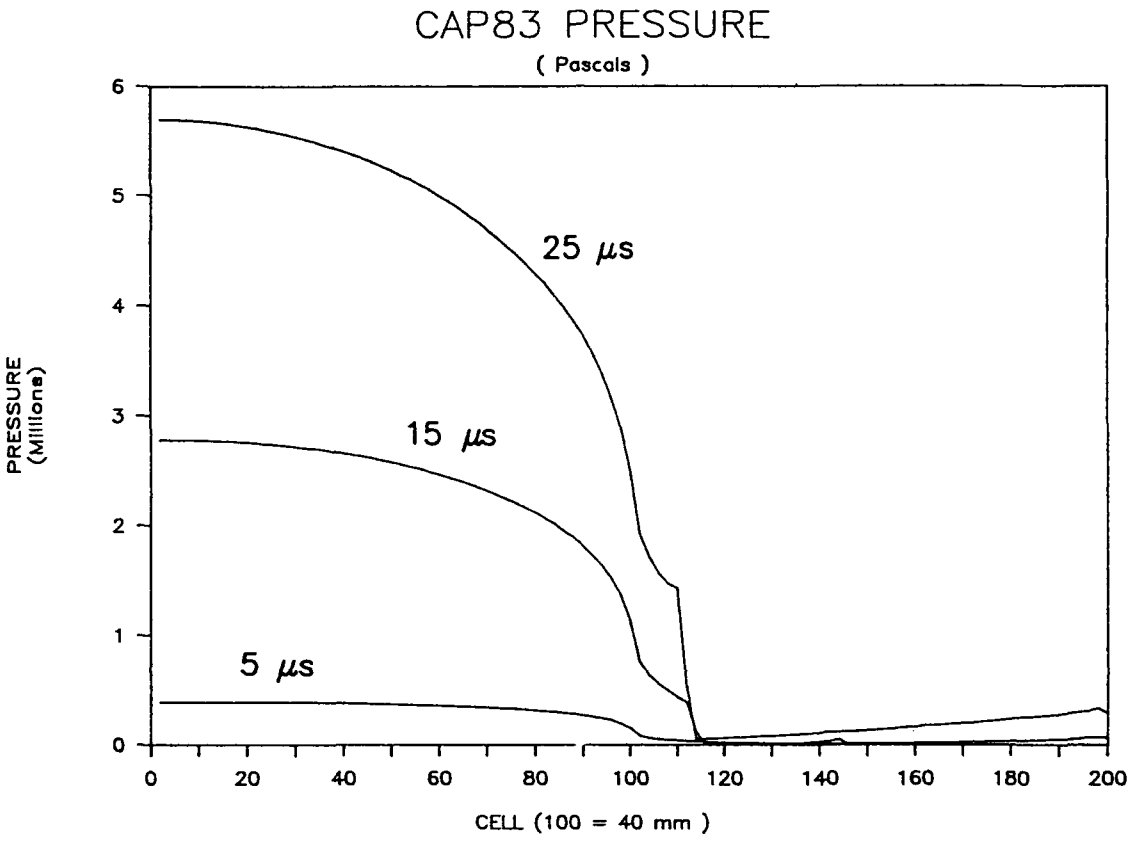

Figure 7.5 - Pressure profiles for water wall injection in a 5 mm capillary at 3 kV (CAP83).

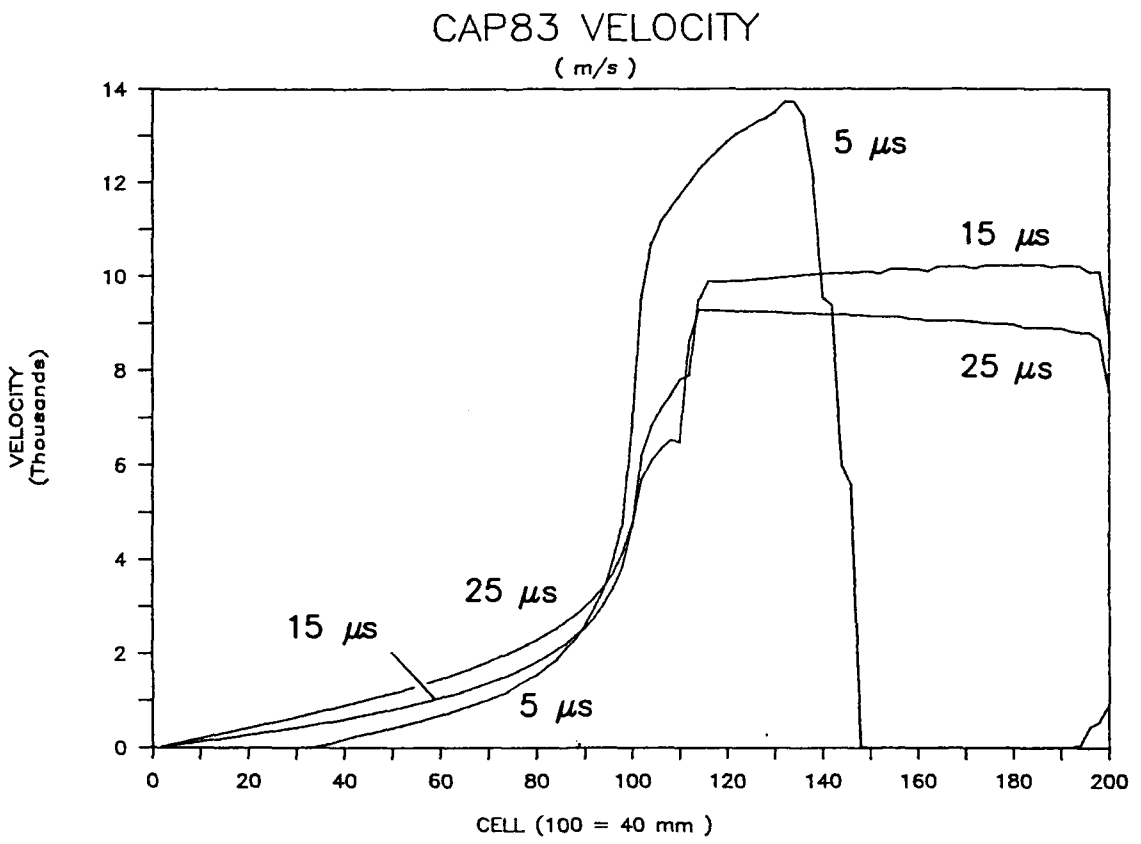

Figure 7.6 - Flow velocity profiles for water wall injection in a 5 mm capillary at 3 kV (CAP83).

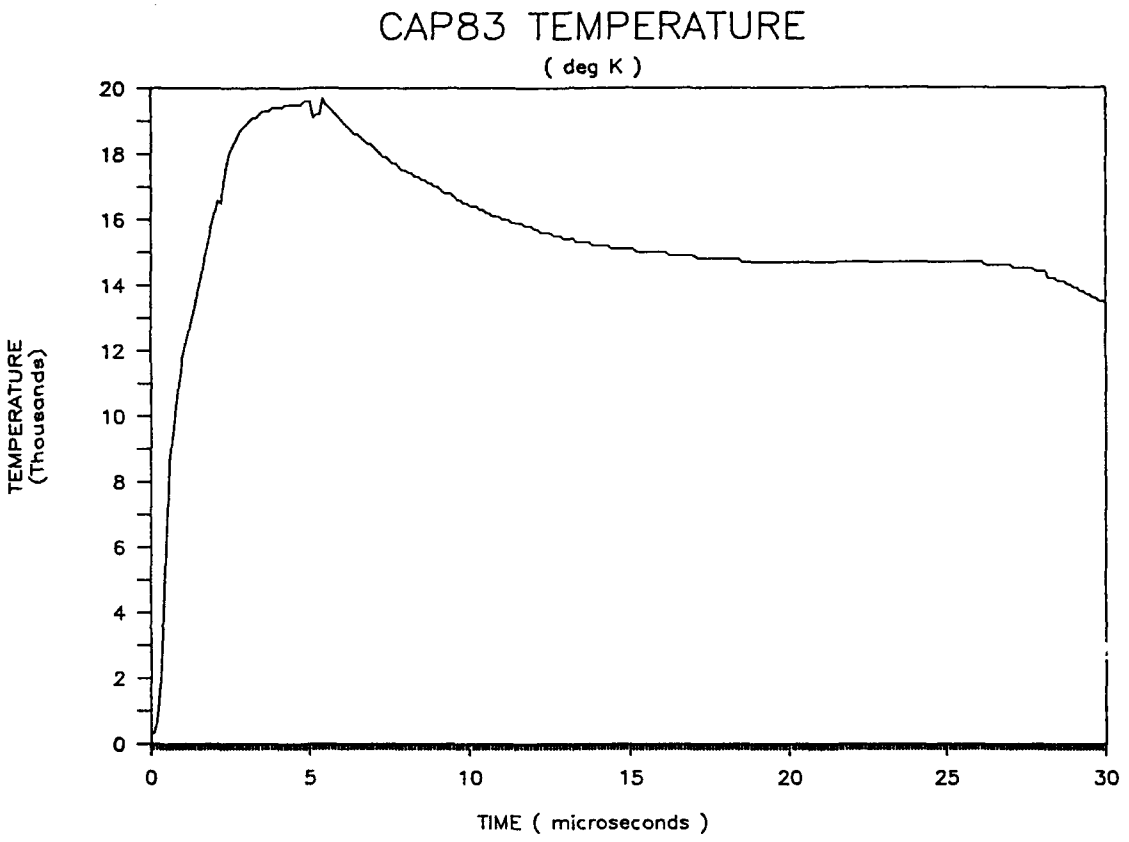

Figure 7.7 - Time dependence of temperature near the cathode (cell 2) for CAP83 simulation.

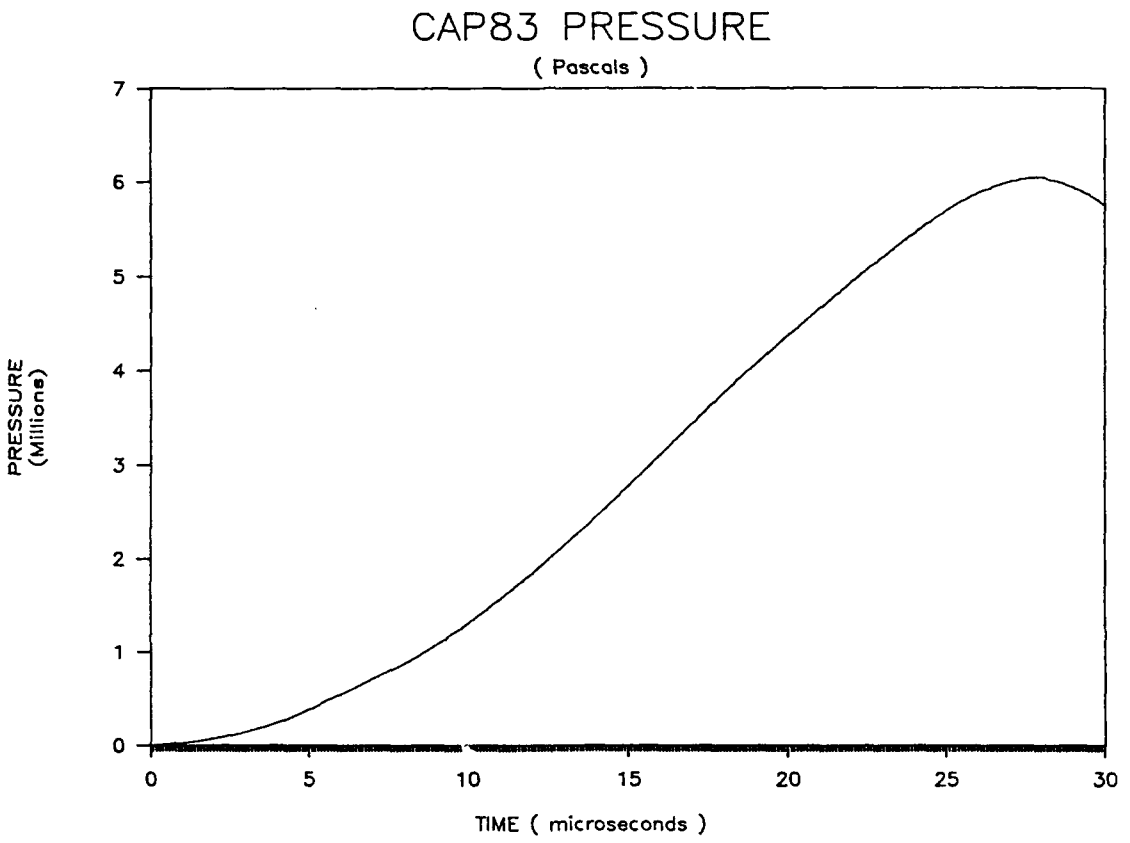

Figure 7.8 - Time dependence of pressure near the cathode (cell 2) for CAP83 simulation.

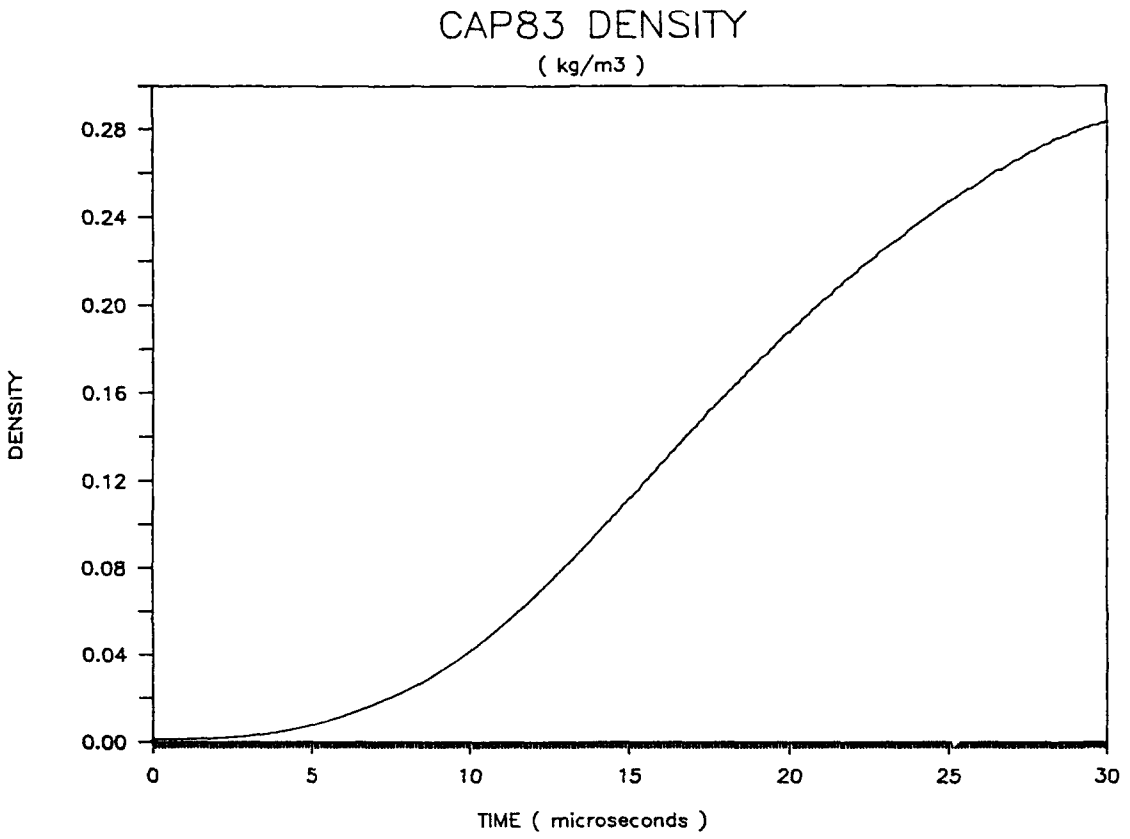

Figure 7.9 - Time dependence of density near the cathode (cell 2) for CAP83 simulation.

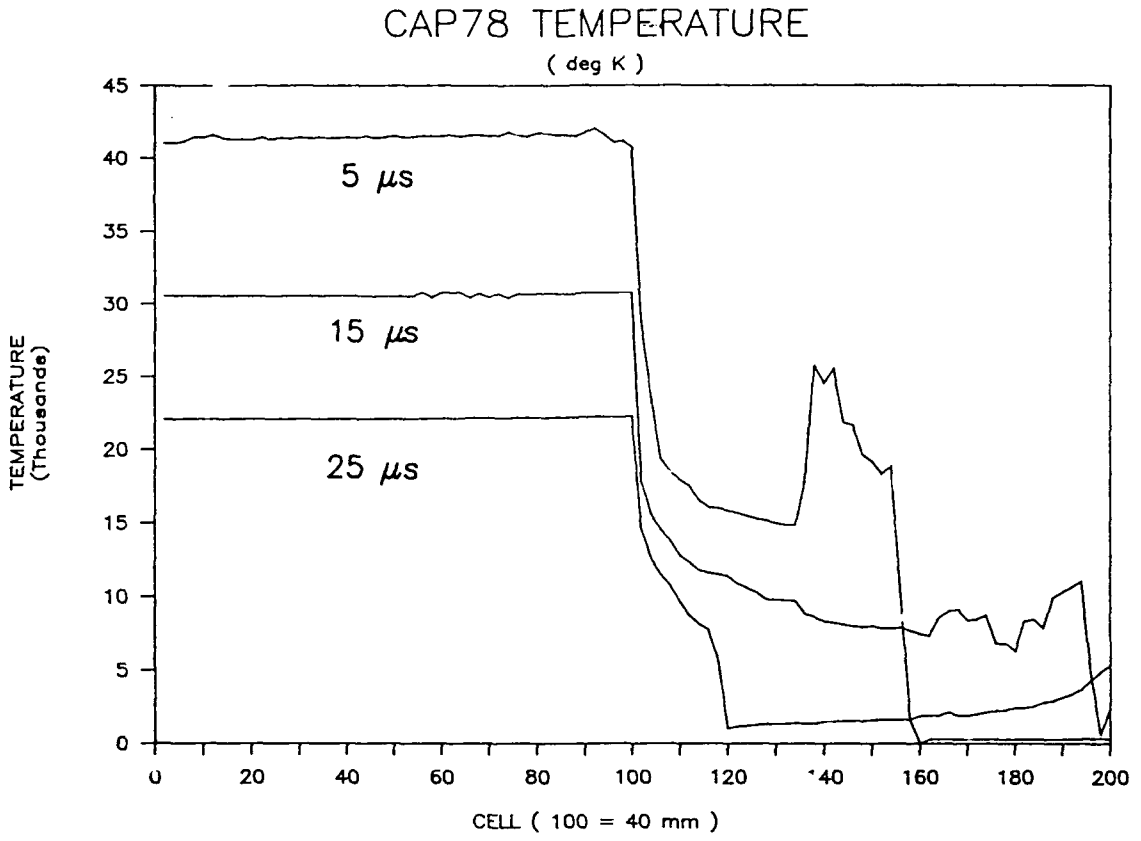

Figure 7.10 - Temperature profiles for straight jet injection in a 5 mm capillary at 3 kV (CAP78).

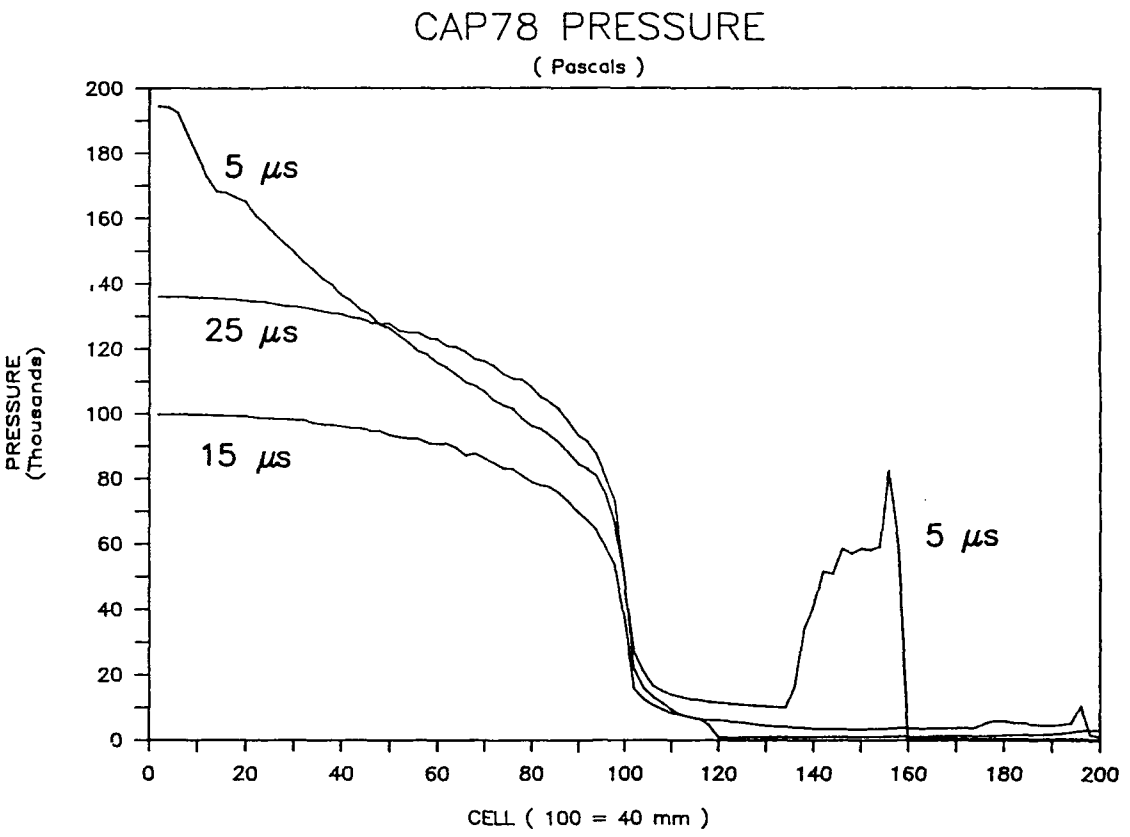

Figure 7.11 - Pressure profiles for straight jet injection in a 5 mm capillary at 3 kV (CAP78).

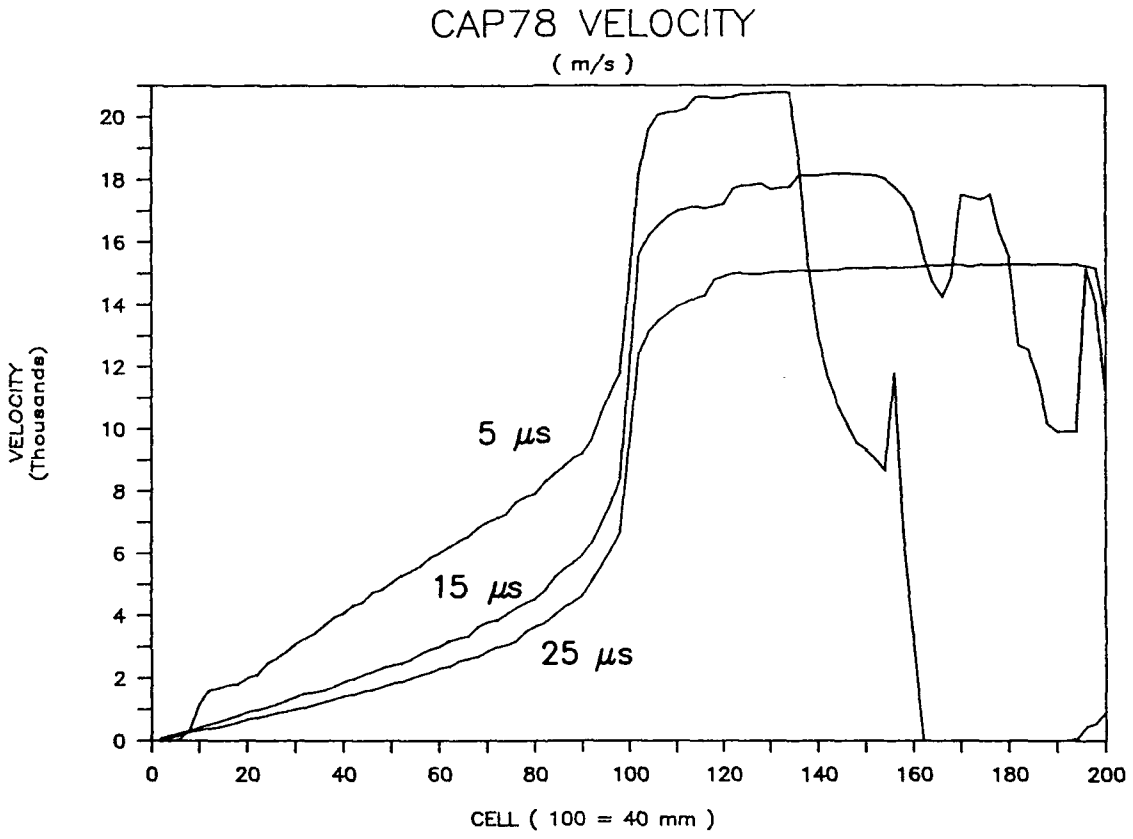

Figure 7.12 - Flow velocity profiles for straight jet injection in a 5 mm capillary at 3 kV (CAP78).

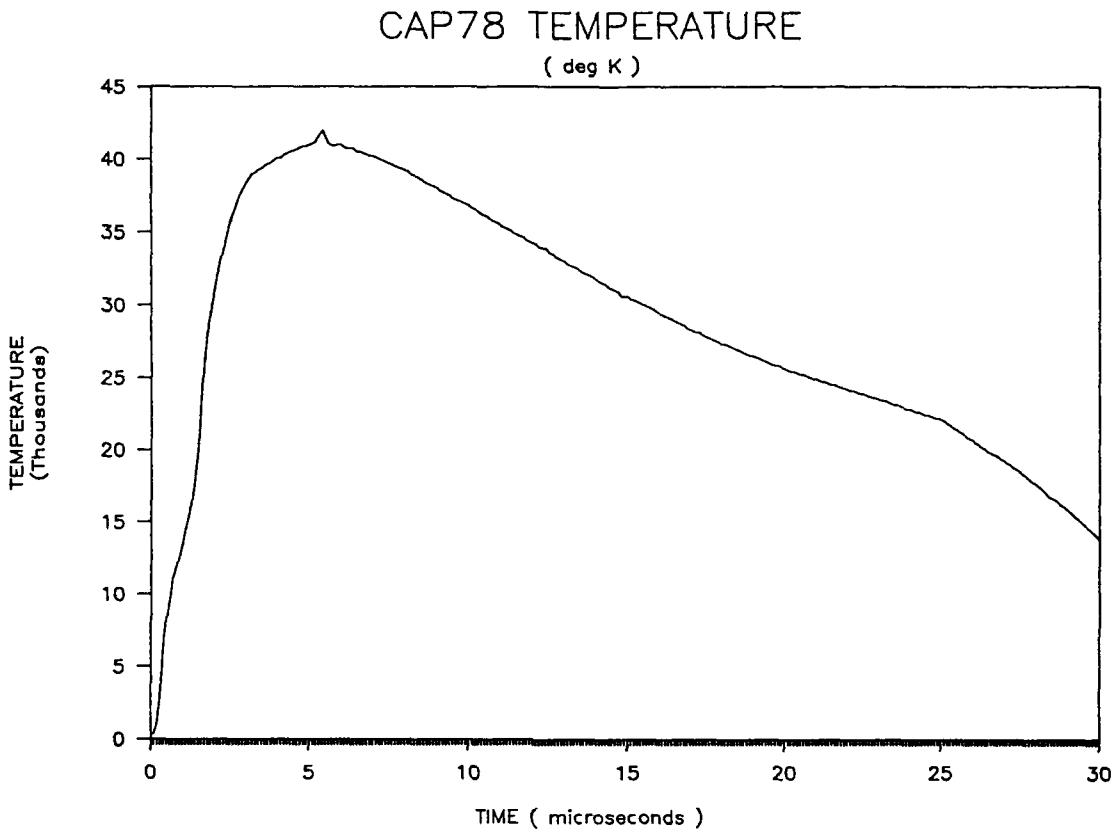

Figure 7.13 - Time dependence of temperature near the cathode (cell 2) for CAP78 simulation.

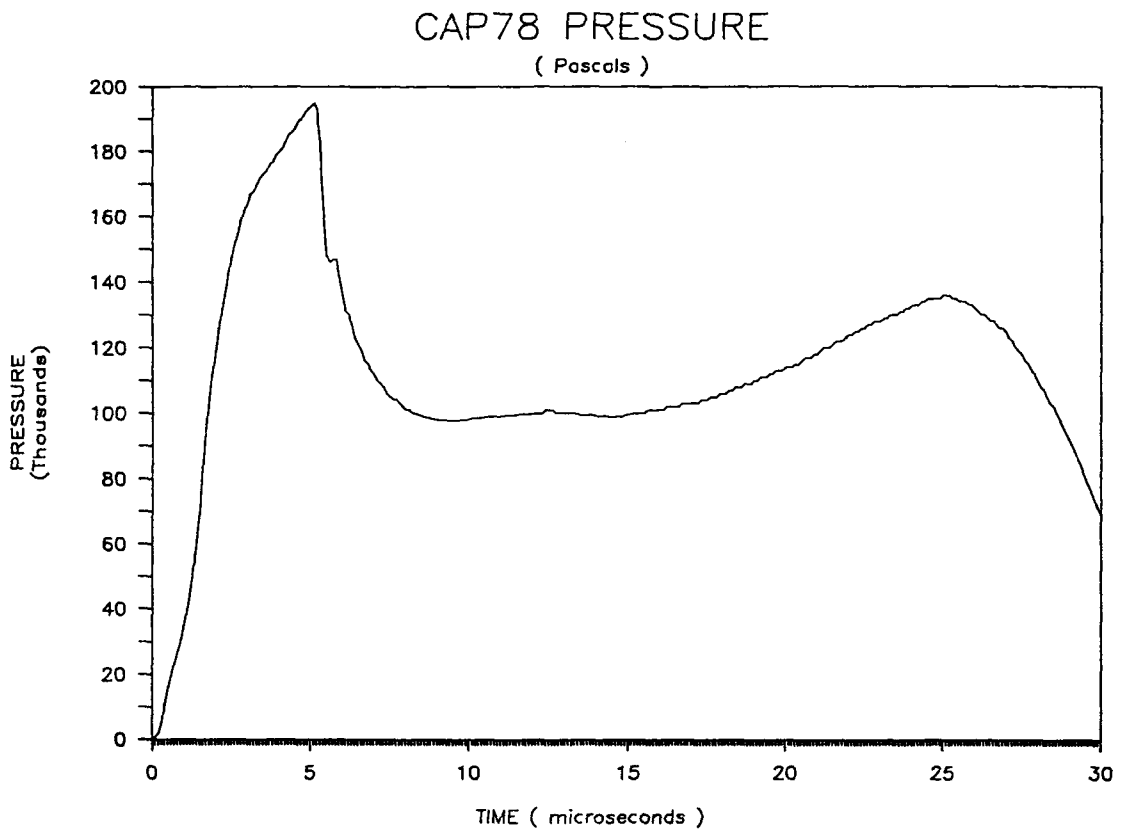

Figure 7.14 - Time dependence of pressure near the cathode (cell 2) for CAP78 simulation.

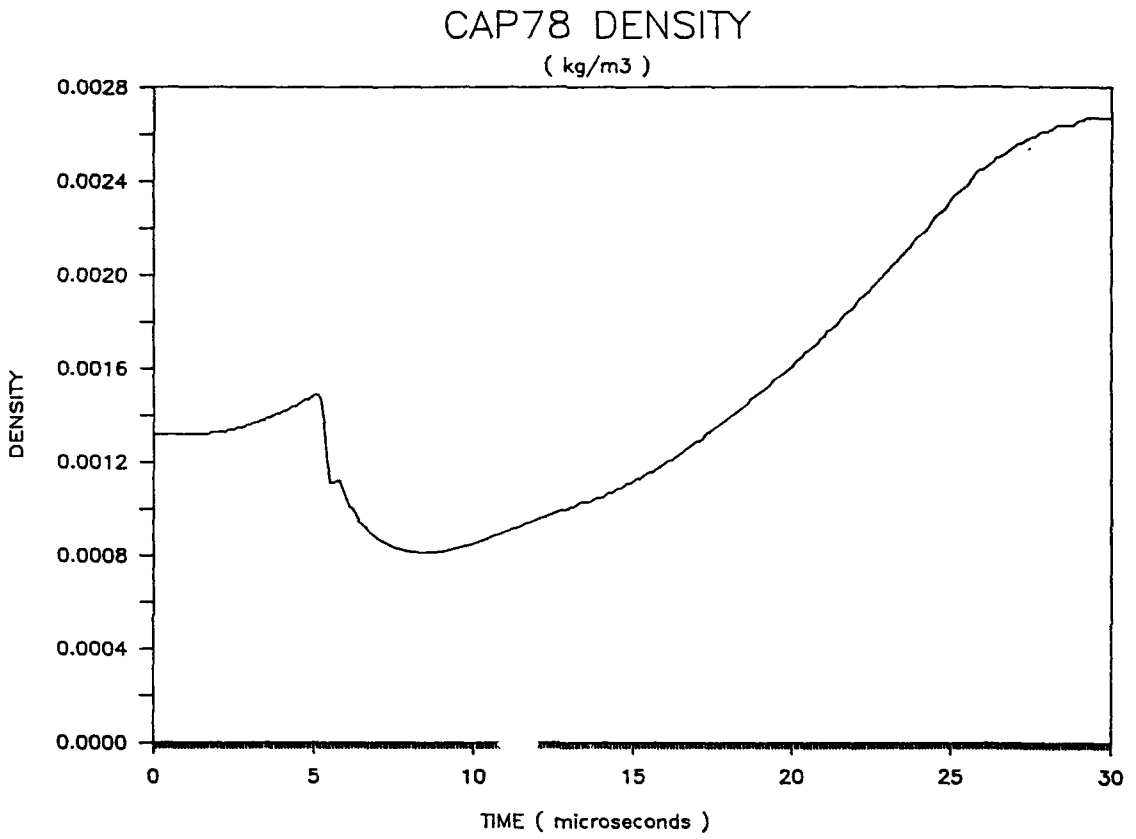

Figure 7.15 - Time dependence of density near the cathode (cell 2) for CAP78 simulation.

7.5 Comparisions to Experiment

The model was evaluated primarily on the basis of its ability to predict capillary resistance. All water injected discharges in the experimental matrix were simulated. In each case, the measured current pulses were used and photodiode signals were obtained to estimate the amplitude functions A(t). Model results are compared to experimental data in Figs. 7.16 and 7.17 for 3 kV and 4 kV charging voltages respectively. The experimental data was reproduced from Fig. 4.1.

Simulations with straight jet injection agree very well with the measurements in terms of both amplitude and shape of the resistance variations. Resistance for the 3.5 mm capillary simulations are consistently higher than experiment by ~15-20%. (It was later discovered that the actual capillary diameter was 3.63 mm which accounts for only about half of the discrepancy.)

In discharges using water wall injection, the ionization levels are very low (1-5%) and electron-neutral resistivity accounts for as much as half of the total. In these cases, uncertainties in the lowering of the ionization potential or electron-neutral collision cross-section can lead to significant differences in resistivity. Measurements for these cases are compared with code runs that do or do not allow for a lowering of the ionization potential. The code runs with $\Delta E_\infty \neq 0$ do appear to follow the resistance modulations more closely in terms of modulation depth and timing. (The straight jet simulations were run with a lowering of the ionization potential. However, since the ionization fraction is large, the results were virtually independent of ΔE_∞.)

Extensive quantitative temperature measurements are only available for the 5 mm capillary using straight jet injection at 3 kV (Sec. 5.2). Nevertheless, these measurements are in complete agreement with the code results (Fig. 7.18).

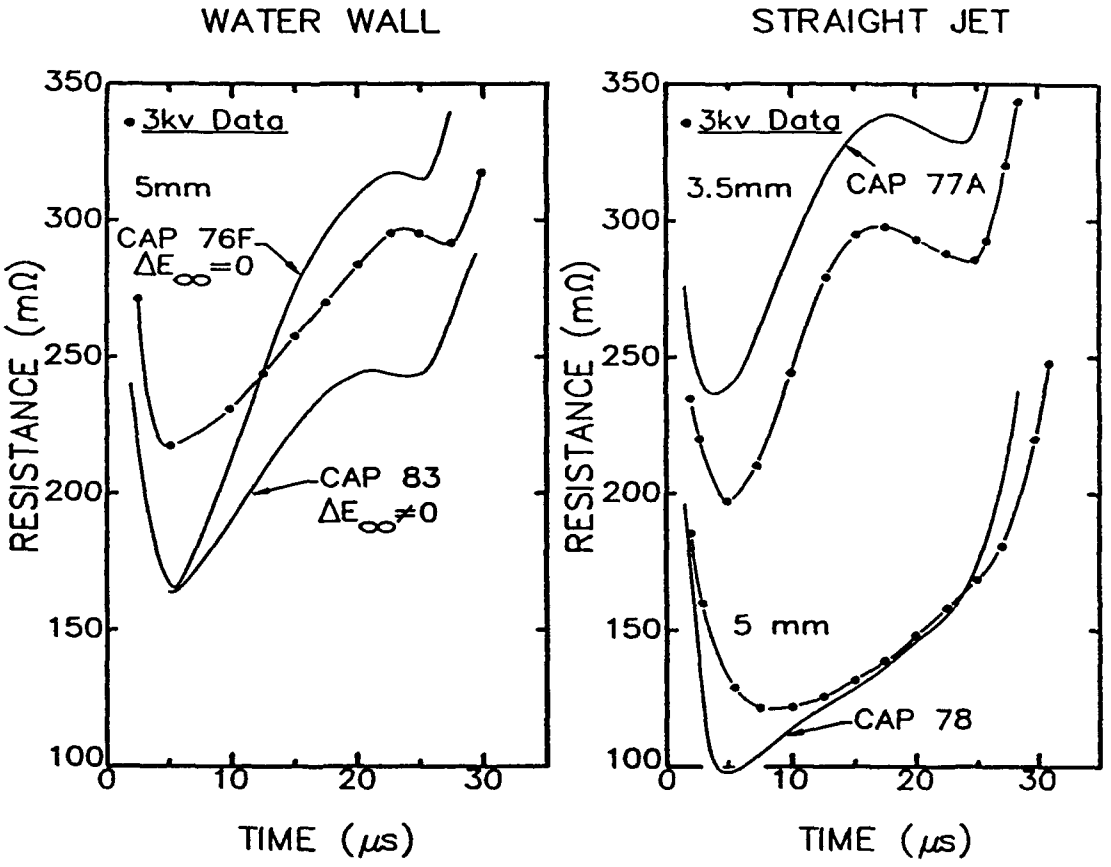

Figure 7.16 - Code predictions of capillary resistance compared to 3 kV experimental data (solid circles).

28A2085

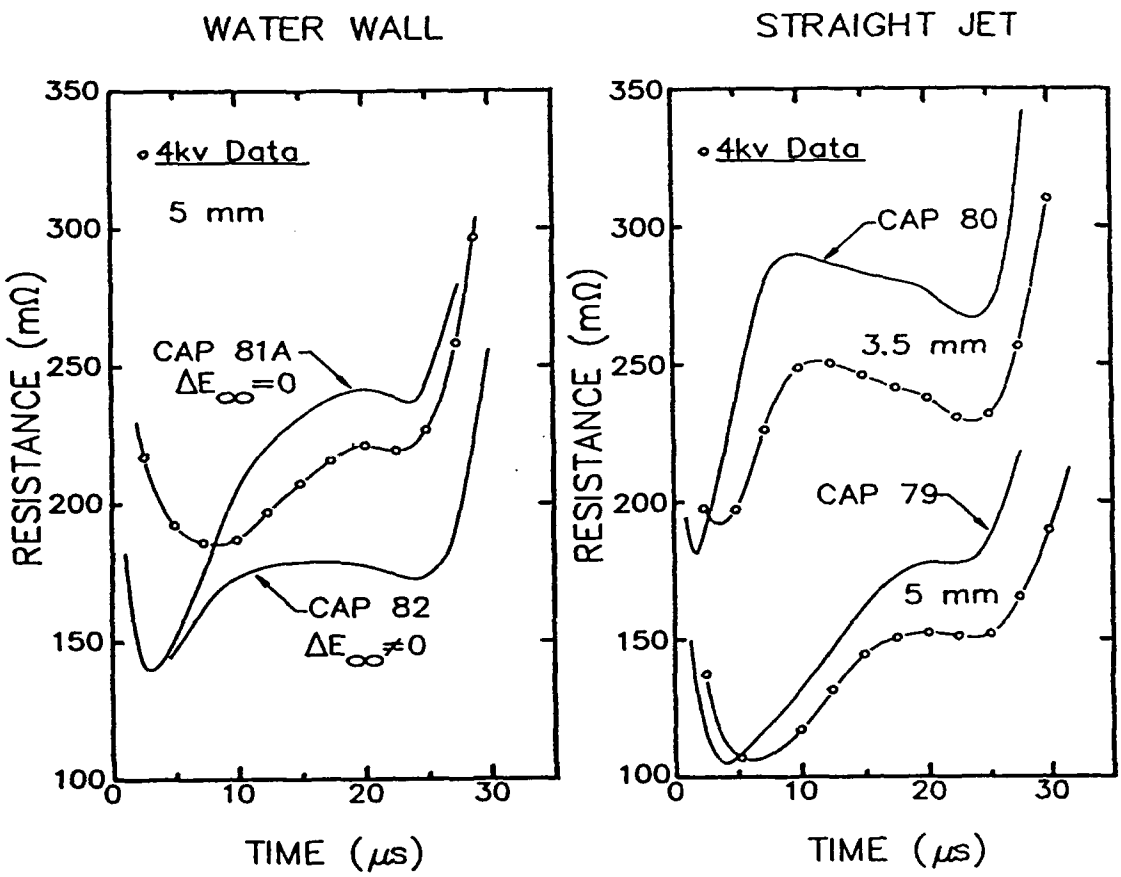

Figure 7.17 - Code predictions of capillary resistance compared to 4 kV experimental data (open circles).

28A2084

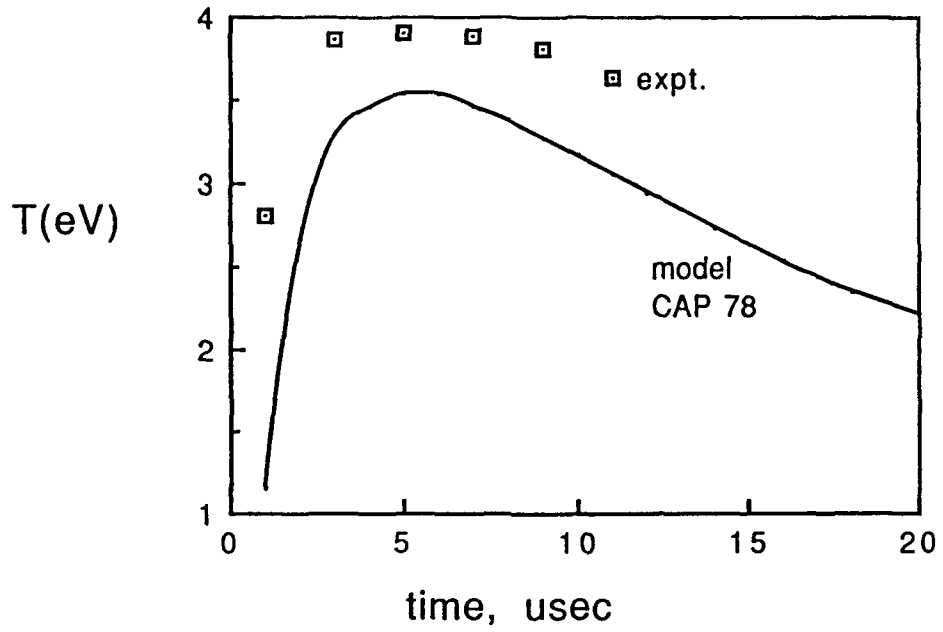

Figure 7.18 - Temperature measurements and code results for the 5 mm capillary with straight jet injection at 3 kV.

8.0 CONCLUSIONS

This study has provided a unique set of observations and experimental data on the dynamic behavior of liquid fuelled capillaries. Detailed resistance measurements reveal the highly transient response of these discharges. Optical diagnostic access has proven difficult though a great deal of semi-quantitative information has been obtained. The optical data collected has given a complete qualitative picture of the radiation response. The spectroscopic and photographic techniques could be extended beyond the limitations of the quartz wall with the use of diamond as a window material. Diamond has excellent thermal conductivity, high melting point, and broadband transmission characteristics and would be well suited to withstand ablation in these harsh plasma environments.

The discharge has been successfully modeled using a simple 1-D description of the vaporization and mixing processes. The model is capable of accurately describing a variety of discharge conditions ranging from hot (~4 eV), low density (~1-10 x 10^{-3} kg/m^3) plasma to cool (~1 eV) plasmas at pressures in excess of 100 atm.

Useful extensions of this work would include a study of longer time scales and how liquid break-up effects the steady state behavior. Also, for applications where efficient fuel utilization is vital, such as the PET thruster, effects due to depletion of fuel during the pulse time can be examined. The model is sufficiently well developed that it can be applied with confidence to further design and optimization studies.

APPENDIX

WATER PLASMA COMPOSITION

This section lays out the equations that were used to determine the species concentrations and thermodynamic functions for a water plasma. Though limited to the temperature and density range of interest for the capillary discharges, these equilibrium calculations appear reasonably accurate and may be of more general interest. Solution of the Saha equations is relatively straightforward and extensive detail is not presented. However, the assumptions and analytic approximations are documented in sufficient detail to reproduce and expand upon the calculations.

In these experiments the temperatures and mass densities being explored lie well within the ranges $0.5 < T < 5.0$ eV and $0.001 < \rho < 0.5$ kg/m^3. The low end of the density range generally represents early stages of the discharge, prior to significant evaporation of water. At such times the specific energy of the plasma can be large resulting in a relatively high temperature (3-5 eV). A high density, low temperature plasma is produced for injection conditions which generate a large surface area for evaporation, such as the water wall type injection. Within the ranges noted it is reasonable to assume that the water is fully dissociated so that no molecular species are considered.[24]

A.1 Equilibrium Equations

The Saha equation for each atomic species, subscript i, can be written as[25]

$$\frac{N_e N_i^{z+1}}{N_i^z} = 2\frac{Q_i^{z+1}}{Q_i^z}\left(\frac{2\pi mkT}{h^2}\right)^{3/2} \exp\{-(E_{i\infty}^z - \Delta E_{i\infty}^z)/kT\} \qquad \text{(A1)}$$

Electrons have number density N_e. Superscripts refer to the charge state with neutral atoms corresponding to $z = 0$. Thus, species of charge z have density N_i^z, electronic partition function Q_i^z, and ionization energy $E_{i\infty}^z$.

In the high density, low temperature regions lowering of the ionization potential can have a significant effect on the degree of ionization. At the same time, in high density plasma the partition functions are not dependent on temperature alone but have some density dependence as well through ΔE. These aspects will be discussed in turn. The initial calculations take $\Delta E = 0$ making the right hand side of Eq. A1 a function of temperature only.

The Saha relation for each atomic species can be cast in the form

$$N_e^{z+1} = N_i^z f_i^z(T)/N_e \,, \tag{A2}$$

where $f_i^z(T)$ is the right hand side of Eq. A1 evaluated at temperature T. Hydrogen and oxygen have i = H and i = O respectively. Charge states up to and including Z = 3 for oxygen are considered. A set of four Saha equations results, one for each of the component densities N_H^0, N_O^0, N_O^1, and N_O^2. This set of equations are expanded with the relations for charge neutrality, composition, and mass comservation, namely

$$N_e = \Sigma Z N_i^z \tag{A3}$$

$$\Sigma N_H^z = 2\Sigma N_O^z \tag{A4}$$

$$\rho/m_p = \Sigma N_H^z + 16\Sigma N_O^z \tag{A5}$$

Equation A4 ensures a stociometric water plasma. In Eq. A5 the plasma has mass density ρ and m_p is the proton mass.

By specifying the temperature and mass density, equations A2-A5 give the particle densities for an equilibrium plasma. The most direct approach is to first solve for the electron density, resulting in the expression

$$N_e^2 = \frac{\rho}{9m_p}\left[\frac{f_H^0}{\left(1 + \dfrac{f_H^0}{N_e}\right)} + \frac{f_O^0\left(1 + 2\dfrac{f_o^1}{N_e} + 3\dfrac{f_o^1 f_o^2}{N_e^2}\right)}{2\left(1 + \dfrac{f_o^0}{N_e} + \dfrac{f_o^0 f_o^1}{N_e^2} + \dfrac{f_o^0 f_o^1 f_o^2}{N_e^3}\right)}\right] \tag{A6}$$

This form for N_e is particularly convenient for iteratively finding N_e. The right hand side is monotonic and smoothly varying so that solutions are easily obtained without any prior knowledge of N_e. It is then straightforward to work backwards through Eqs. A2-A5 to obtain the remaining densities.

A.2 Partition Functions

The electronic partition functions were calculated on the bases of Moore's tabulations of atomic levels.[26] The partition functions are very well defined for temperatures below about 3 eV. For temperatures between 3-5 eV all energy levels up to within a few percent of the ionization energy were taken into account. Estimates for the contribution of high lying quasi-continuum levels have been suggested[27] but such refinements were not incorporated in the present calculations. Imposing a small but more-or-less arbitrary cut-off to the summation does in effect presuppose a lowering of the ionization potential by some fixed value that is independent of both temperature and density. This is not a severe restriction since the dominant influence of ΔE appears in the Boltzman factor in Eq. A1.

The partition functions for each species were calculated at several temperatures within the range of interest and simple analytic fits were made to the data. Table A1 lists the resulting functions used for Q(T) when T is expressed in electron volts.

Table A1 Analytic forms used for the electronic partition functions of hydrogen and oxygen.

Species	Q(T) - T in eV
HI	$2.000 + 787.43\exp(-12.81/T)$
HII	1.0
OI	$8.880 + 0.0161T^2 + 0.3657T^3$
OII	$3.790 + 0.6450T^2 - 0.0378T^3$
OIII	$8.750 + 0.4870T^2 - 0.0497T^3$
OIV	$5.730 + 0.0765T^2 + 0.0076T^3$

A.3 Reduction of the Ionization Potential

In cases of low temperature and high density, notably those with water wall injection conditions, the plasma may have a fractional ionization of only a few percent. Under these circumstances the resistivity calculations were found to be quite sensitive to the ion-to-neutral density ratio and it was necessary to account to some degree for a lowering of the ionization potential.

Two effects are usually considered in estimating the magnitude of ΔE, namely plasma polarization and lattice effects. Essentially an electron is considered free of its atom or ion

when it is excited to a quantum level whose mean orbital radius exceeds the Debye shielding distance (plasma polarization term) or the average interparticle spacing (lattice term). Several estimates for ΔE have been made[11,28] though there is some dissagreement as tc the magnitude of the effects. Here we have used the the following expression to obtain ΔE in units of electron volts,

$$\Delta E = 1.44 \times 10^{-9} (2.78/r_o + 0.65/r_D) , \qquad (A7)$$

where the interparticle separation, r_o, and Debye radius, r_D, are given in meters. Equation A7 uses the average value of the Debye and lattice terms tabulated in Ref. 11. The interparticle separation is $r_o = (3/4\pi N)^{1/3}$ where the total particle density N is taken to be

$$N = N_e + \Sigma N_i^z .$$

The Debye radius is given by

$$r_D = \left[\frac{\epsilon_o kT}{e^2(N_e + \Sigma Z^2 N_i^z)} \right]^{1/2}$$

where k is Boltzman's constant, ϵ_o the free space permittivity, and e the elementary charge.

Throughout the range of plasma conditions being considered the lattice term is the dominant factor in determining ΔE. As an example, the magnitude of the ionization potential lowering for a protonic plasma with $N_e = 2 \times 10^{18}$ cm^{-3}, T = 2 eV is 1.02 eV and 0.18 eV for the lattice and Debye terms respectively.

Figure A1 plots the calculated ionization fraction, α, for a water plasma. Alpha is the mean charge of the heavy particles, defined here as

$$\alpha = N_e/\Sigma N_i^z .$$

At low density ΔE has negligable effect on α. The strongest effects are seen in the high density, low temperature data where fractional ionizaton increases by factors of 2-3 with the inclusion of ΔE.

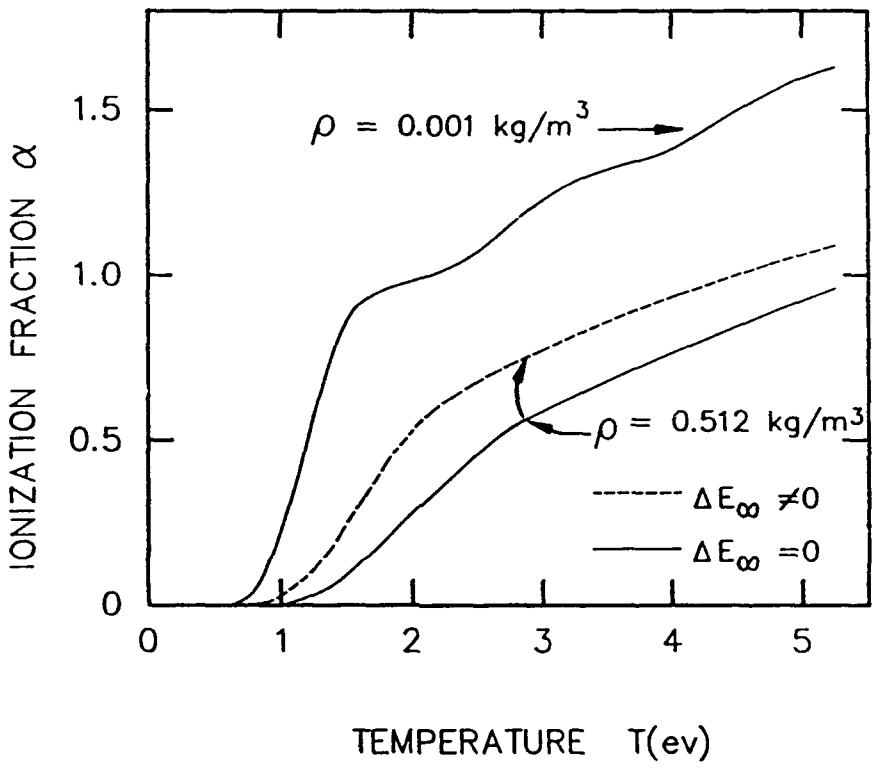

Figure A1 - Fractional ionization calculated for an equilibrium water plasma.

28A2083

A.4 Thermodynamic Quantities

Given the equilibrium composition we can define various macroscopic quantities used to describe the plasma state. The definitions that were used in the capillary modelling are summarized as follows.

The plasma is treated as an ideal gas with total pressure being the sum of all partial pressures,

$$P = kT(N_e + \Sigma N_i^z) \ .$$

The mean charge of the ions is taken to be

$$<z> = \Sigma N_i^z / N_e \ ,$$

where the summation here extends over the ions only.

The internal energy of the plasma is calculated as

$$w = (W_K + W_I + W_E)/\rho$$

using the three primary sources, kinetic W_K, ionization W_I, and electronic excitation W_E, energies. Here the mass density ρ(g/cm^3) relates the specific internal energy w(J/g) to the internal energy density W(J/cm^3). The contributing terms are

$$W_K = 1.5kTN \ ,$$

$$W_I = \Sigma N_i^z (E_{i\infty}^{z-1} - \Delta E_{i\infty}^{z-1}) \ , \textit{and}$$

$$W_E = kT^2 \Sigma N_i^z \frac{\partial ln Q_i^z}{\partial T} \ .$$

The analytic forms of the partition functions, as given in Table A1, are used to calculate the exitation energies of the various species. Recall that complete dissociaton has been assumed so that molecular contributions to the internal energy have been ignored. In particular, the dissociation energy per water molecule, totalling 9.63 eV, is neglected in W. However, for temperatures larger than about 1 eV the dissociation energy contributes only a few percent to the total internal energy.

Other quantities used in the model calculations are the specific enthalpy $h = w + P/\rho$ and the enthalpy coefficient g which is defined as $g = h/w$, or alternatively through the expression

$$h = \frac{g}{g-1} (P/\rho) .$$

Figure A2 gives the calculated enthalpy coefficient for various conditions. The values of g for temperatures below about 1 eV should be treated with some caution since, as noted above, the dissociation energy has not been taken into account.

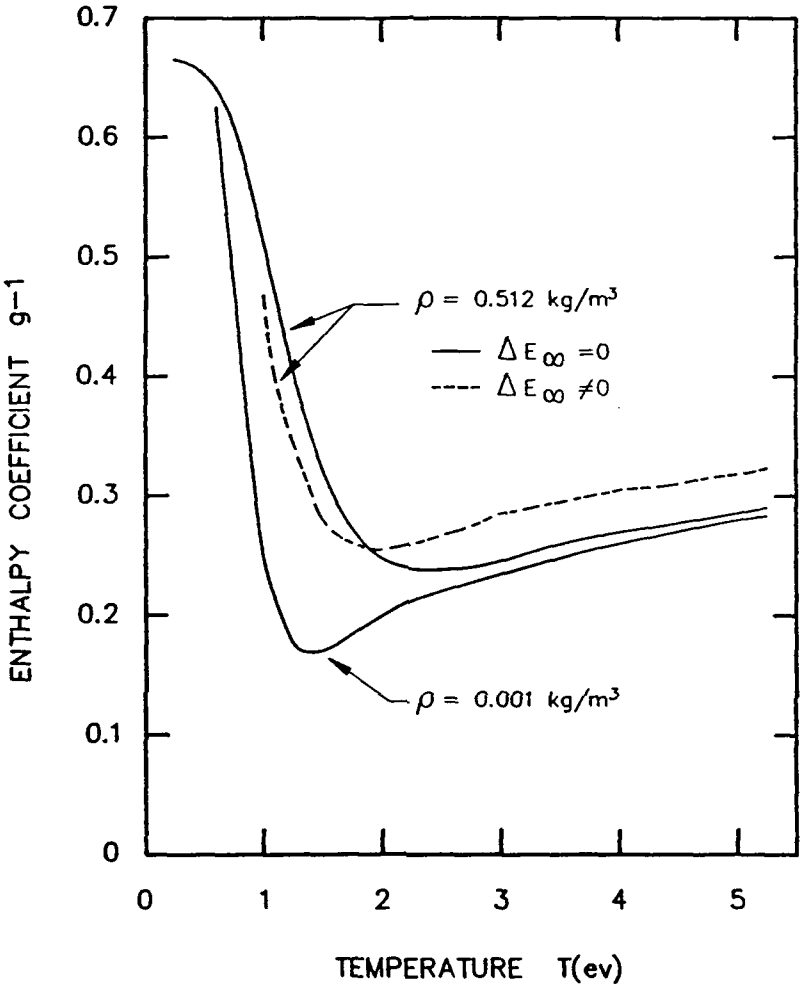

Figure A2 - Enthalpy coefficient calculated for an equilibrium water plasma.

28A2082

REFERENCES

1. R.L. Burton, D. Fleischer, S.A. Goldstein, D.A. Tidman, and N.K. Winsor, "Investigation of a Repetitive Pulsed Electrothermal Thruster," GT-Devices, Inc., Report No. GTD 86-5, NASA CR-179464, Lewis Research Center, August 21, 1986.

2. R.L. Burton, S.A. Goldstein, and G.G. Geelan, "Liquid Arc Heater for National Aerospace Plane Testing at High Mach Numbers," GT-Devices, Inc., Tech. Note No. GTD 88-3, March 1, 1988.

3. R.L. Burton, W. Chinitz, O. Rizkalla, and F.D. Witherspoon, "High Pressure Mach 10-20 Electrothermal Hypersonic Wind Tunnel," presented at the JANNAF Propulsion Meeting, Anaheim, CA., October, 1990.

4. R.L. Burton and B.K. Hilko, "Heating of a Liquid/Vapor Mixture by a Pulsed Electric Discharge," GT-Devices, Inc., Report No. GTD 88-8, AFOSR Contract No. F49620-87-C-0061, July 31, 1988.

5. R.L. Burton, B.K. Hilko and F.D. Witherspoon, "Heating of a Liquid/Vapor Mixture by a Pulsed Electric Discharge," GT-Devices, Inc., Report No. GTD 89-9, AFOSR Contract No. F49620-87-C-0061, July 31, 1989.

6. The time of appearance of silicon emission was used previously to estimate the heat flux to the wall.[4] Under the conditions described the mean heat flux q ~ 250 kW/cm^3 during the first 4 μs.

7. T. Efthymiopoulos and K. Garside, "High-Energy Short-Pulse Flashlamps: Operating Characteristics," *Applied Optics*, *16*(1), 70-76 (1977).

8. W. Lochte-Holtgreven, in Plasma Diagnostics, edited by W. Lochte-Holtgreven (John Wiley & Sons, New York, 1968), Chap. 3, pp. 178-183.

9. H.R. Griem, Plasma Spectroscopy, (McGraw-Hill, New York, 1964), Chap. 13, pp. 267-279.

10. W.H. Wiese, M.W. Smith, and B.M. Glennon, Atomic Transition Probabilities, Nat. Stand. Ref. Data Series, NSRDS-NBS 4 (Nat. Bur. Stand., Washigton, D.C., 1966), Vol. I.

11. W. Lochte-Holtgreven, in Plasma Diagnostics, edited by W. Lochte-Holtgreven (John Wiley & Sons, New York, 1968), Chap. 3, pp. 156-157.

12. G.W. LeCompte and H.E. Edgerton, "Xenon Arc Transients, Electrical and Optical," J. Appl. Phys. 27(12), 1427-1430 (1956).

13. M. Autric, P. Vigliano, D. Dufresne, J.P. Caressa, and Ph. Bournot, "Pulsed CO_2 Laser-Induced Effects on Water Droplets," AIAA Journal, 26 (1), 65-71 (1988).

14. G.M. Faeth, "Evaporation and Combustion of Sprays," in Progress in Energy and Combustion Science, 9, 1-76 (1983).

15. A.H. Nayfeh and D.T. Mook, "Nonlinear Stability of a Liquid Adjacent to a Supersonic Stream," Phys. Fluids, 16 (12), 2089-2091 (1973).

16. D.A. Tidman and S.A. Goldstein, "Thermal Transport to Hypervelocity Gun Tubes by High Pressure Partially Ionized Gas Flows," GT-Devices, Inc., Tech. Note No. GTD 85-4, May, 1985.

17. D.A. Tidman, Y.C. Thio, S.A. Goldstein, and D.S. Spicer, "High Velocity Electrothermal Mass Launchers," GT-Devices, Inc., Tech. Note No. GTD 86-7, November, 1986.

18. C.B. Ruchti and L. Niemeyer, "Ablation Controlled Arcs," IEEE Trans. Plasma Sci., PS-14 (4), 423-434 (1968).

19. D.A. Tidman, S.A. Goldstein, and N.K. Winsor, "A Rail Gun Plasma Armature Model," GT-Devices, Inc., Tech. Note No. GTD 86-3, March, 1986.

20. D.L. Book, NRL Plasma Formulary, (Naval Research Laboratory, Washington, D.C., 1978).

21. L. Spitzer, Physics of Fully Ionized Gases, 2nd ed. (John Wiley and Sons, New York, 1962), pp. 138-139.

22. J.P. Boris and D.L. Book, "Flux-Corrected Transport. I. SHASTA, A Fluid Transport Algorithm That Works," J. Comput. Phys., 11, 38-69 (1973).

23. R.L. Burton, N.K. Winsor, and F.D. Witherspoon, "Numerical Modeling of Fully Viscous Rocket Plume Flows," GT-Devices, Inc., Report No. GTD 88-9, Contract No. NAS 3-25407, NASA-Lewis Research Center, August 26, 1988.

24. J. Richter, in Plasma Diagnostics, edited by W. Lochte-Holtgreven (John Wiley & Sons, New York, 1968), Chap. 1, pp. 18-19.

25. H.R. Griem, Plasma Spectroscopy, (McGraw-Hill, New York, 1964), Chap. 6, pp. 134-137.

26. C.E. Moore, Atomic Energy Levels, Nat. Bur. Stand.(U.S.), Circ. 467, Vols. I, II, III.

27. H.R. Griem, Plasma Spectroscopy, (McGraw-Hill, New York, 1964), Chap. 6, pp. 140-142.

28. G. Ecker and W. Kroll, "Lowering of the Ionization Energy for a Plasma in Thermodynamic Equilibrium," Phys. Fluids 6(1), 62-69 (1963).